

# Targeting Oncogene Promoters and Ribosomal RNA Biogenesis by G-Quadruplex Binding Ligands Translate to Anticancer Activity

Yelisetty Venkata Suseela,<sup>||</sup> Pallabi Sengupta,<sup>||</sup> Tanaya Roychowdhury,<sup>||</sup> Suman Panda, Sangita Talukdar, Samit Chattopadhyay, Subhrangsu Chatterjee,\* and Thimmaiah Govindaraju\*



Cite This: *ACS Bio Med Chem Au* 2022, 2, 125–139



Read Online

ACCESS |

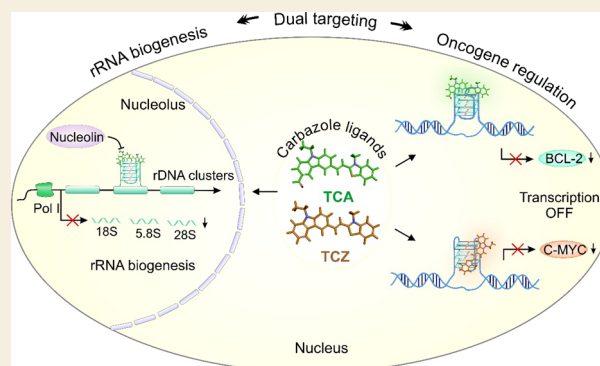
Metrics & More

Article Recommendations

Supporting Information

**ABSTRACT:** G-Quadruplex (GQ) nucleic acids are promising therapeutic targets in anticancer research due to their structural robustness, polymorphism, and gene-regulatory functions. Here, we presented the structure–activity relationship of carbazole-based monocyamine ligands using region-specific functionalization with benzothiazole (TCA and TCZ), lepidine (LCA and LCZ), and quinaldine (QCA and QCZ) acceptor moieties and evaluated their binding profiles with different oncogenic GQs. Their differential turn-on fluorescence emission upon GQ binding confirmed the GQ-to-duplex selectivity of all carbazole ligands, while the isothermal titration calorimetry results showed selective interactions of TCZ and TCA to *c-MYC* and *BCL-2* GQs, respectively. The aldehyde group in TCA favors stacking interactions with the tetrad of *BCL-2* GQ, whereas TCZ provides selective groove interactions with *c-MYC* GQ. Dual-luciferase assay and chromatin immunoprecipitation (ChIP) showed that these molecules interfere with the recruitment of specific transcription factors at *c-MYC* and *BCL-2* promoters and stabilize the promoter GQ structures to inhibit their constitutive transcription in cancer cells. Their intrinsic turn-on fluorescence response with longer lifetimes upon GQ binding allowed real-time visualization of GQ structures at subcellular compartments. Confocal microscopy revealed the uptake of these ligands in the nucleoli, resulting in nucleolar stress. ChIP studies further confirmed the inhibition of Nucleolin occupancy at multiple GQ-enriched regions of ribosomal DNA (rDNA) promoters, which arrested rRNA biogenesis. Therefore, carbazole ligands act as the “double-edged swords” to arrest *c-MYC* and *BCL-2* overexpression as well as rRNA biogenesis, triggering synergistic inhibition of multiple oncogenic pathways and apoptosis in cancer cells.

**KEYWORDS:** G-quadruplex, turn-on fluorescence, anticancer activity, oncogene, ribosome biogenesis, therapeutics



## INTRODUCTION

Noncanonical G-quadruplex (GQ) nucleic acid structures have emerged as appealing intracellular targets for therapeutic intervention in anticancer research.<sup>1</sup> GQs are formed over several repeats of adjacent guanine-rich sequences comprising a stem of  $\pi$ - $\pi$  stacked guanine-tetrads in a coplanar fashion that cohere through Hoogsteen hydrogen bonds involving N1, N7, O6, and N2 of guanine bases. GQ structures fold naturally under physiological pH and are highly stabilized as the central carbonyl-O6 offers metal cation ( $\text{Na}^+$  or  $\text{K}^+$ ) coordination.<sup>2,3</sup> They are widely present at the consensus regions of human genome, *viz.*, telomeres, promoters, open reading frames, and untranslated regions of the oncogenes, ribosomal DNA, and translocation hotspots.<sup>1,4</sup> They regulate the fidelity of gene expression pathways and are implicated in genomic instability, telomerase dysfunction, oncogene transcriptions, ribosomal RNA biogenesis,<sup>5</sup> and tumorigenesis.<sup>6–8</sup>

Over the past two decades, significant research has converged on the development of optical probes for the

intracellular detection of GQ structures.<sup>9,10</sup> To date, GQ-specific antibodies, such as BG4<sup>11</sup> and 1H6,<sup>12</sup> and high-throughput sequencing<sup>13</sup> have provided direct evidence for intracellular GQ mapping in human chromosomes. However, the dynamic relationships between GQ formation and cellular functions are poorly understood.<sup>14,15</sup> The common cross-linking and fixation methods change the cytoplasmic density, resulting in a damaged organelle and the extraction of nuclear proteins, which perturb real-time monitoring of GQ dynamics.<sup>16,17</sup> Moreover, antibody-based GQ staining allows only high GQ density domains to form fluorescent foci while the detection of the low GQ density domains is limited by spatial

**Received:** September 16, 2021

**Revised:** November 11, 2021

**Accepted:** November 12, 2021

**Published:** November 22, 2021



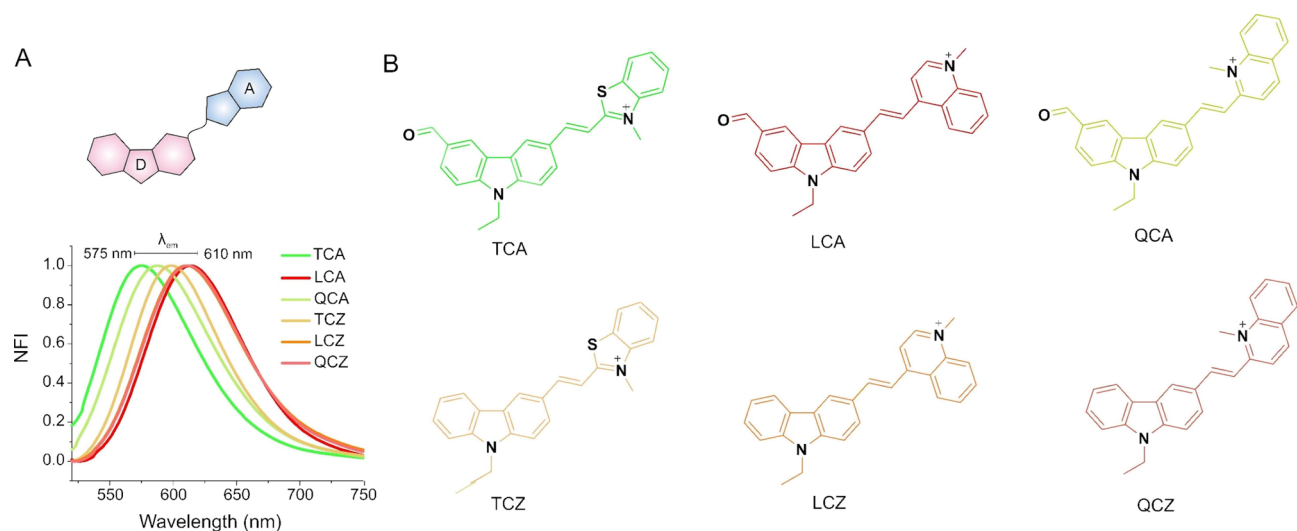


**Figure 1.** Design of carbazole derivatives. (A) Chemical structures of carbazole-based monocyanyne derivatives with a donor D carbazole moiety appended to various acceptor A moieties resulting in (B) TCA, LCA, QCA, TCZ, LCZ, and QCZ. Left panel: Normalized fluorescence intensity (NFI) of carbazole derivatives measured in 20 mM PBS, 100 mM KCl, pH 7.4, at 24 °C.  $\lambda_{em}$ , maximum fluorescence emission wavelength of carbazole ligands.

resolution.<sup>18</sup> In this context, cell membrane-permeable small molecule fluorescent probes that specifically recognize cellular GQs circumvent the limitations of fixed cell artefacts and offer powerful and direct means of probing their dynamic folding and subcellular localization in live cells.<sup>14,19,20</sup> In recent times, various fluorescent probes are developed to detect cytoplasmic RNA<sup>21,22</sup> and DNA GQs in subcellular organelles of live cells,<sup>23–26</sup> but, their applications are limited by the off-target effects, raising an unmet need for the development of GQ-specific fluorescent probes that offer dynamic monitoring of GQ targets in live cells with reduced off-target effects.

*c-MYC* and *BCL-2* are two pleiotropic oncogenes that orchestrate many biochemical processes including autonomous proliferation, replication, apoptosis, increased protein biogenesis, cellular metabolism, angiogenesis, and chemoresistance.<sup>27,28</sup> Their constitutive activation in human cancers serves as the nodal points of multiple signaling pathways.<sup>29,30</sup> Recently, the World Health Organization (WHO) appraised the coexpression of *c-MYC* and *BCL-2* as the prognostic markers in lymphoma,<sup>31,32</sup> suggesting them as the promising targets in anticancer therapeutics. To date, a handful of *c-MYC*- and *BCL-2*-targeted therapeutic strategies showed remarkable advances in the preclinical and clinical trials<sup>33,34</sup> but is limited due to the “undrugability” of *c-MYC* proteins,<sup>35</sup> acquired resistance,<sup>36,37</sup> genetic mutations, and constitutive activation of the downstream signaling cascades. *c-MYC* and *BCL-2* promoters are the repositories of transcription-silencing GQ scaffolds that serve as the anti-neoplastic targets. *c-MYC* oncogene harbors a 27-mer GQ-forming element (Pu27) in the nuclease hypersensitive element (NHE) III<sub>1</sub> located –142 to –115 base pairs upstream of the *c-MYC*-P<sub>1</sub> promoter that controls 80–90% of its transcription.<sup>38</sup> Likewise, a 39-mer GQ-motif (Pu39), located at 58–19 bp upstream of the *BCL-2*-P<sub>1</sub> promoter inhibits *BCL-2* transcription in the cells.<sup>39,40</sup> Therapeutic implications of these GQs gained a momentum with the revelation that upregulated transcriptions of *c-MYC* and *BCL-2* can be inversely regulated by stabilizing these GQ motifs by small molecules, which sensitize the cancer cells to apoptotic death.<sup>41,42</sup> In this connection, the rational design of the fluorescent molecules showing a high-affinity interaction

with *c-MYC* and *BCL-2* GQs is a promising approach for the real-time detection of intracellular GQ dynamics and therapeutic activity.

Despite significant progress in developing GQ-interactive small molecular probes, acquired resistance is one of the major limitations for small molecule-based therapeutic strategies.<sup>43</sup> Enhanced ribosomal RNA biogenesis promotes a proliferative advantage in cancer cells with increased translation competence.<sup>44</sup> Overexpression of ribosomal proteins have a pivotal influence on tumorigenesis and acquired chemoresistance, driving the cancer cells to escape apoptosis.<sup>45,46</sup> The oncogenic potential of *c-MYC* relies on its ability to enhance rRNA biogenesis and protein synthesis.<sup>47,48</sup> In hepatic carcinoma, ribosomal proteins drive IRES (internal ribosome entry site)-dependent *c-MYC* translation that accounts for stress resistance.<sup>49,50</sup> In this connection, a GQ-based dual-targeting approach provides a preclinical proof-of-concept suggesting that oncogenic GQ-interactive small molecules might effectively overcome rRNA biogenesis-induced resistance in cancer cells.

Encouraged by the wealth of knowledge on the design and use of GQ-selective small molecules as anticancer agents,<sup>10,51,52</sup> we have undertaken a structure–activity investigation of carbazole-based monocyanyne ligands by functionalizing with various electron-accepting moieties and demonstrated their *in cellulo* GQ selectivity at oncogene promoter levels besides GQ visualization in live cells and therapeutic potential. Earlier reports have shown that carbazole-based biscyanine derivatives, for example, 3,6-bis(1-methyl-4-vinylpyridinium) carbazole diiodide (BMVC), exhibit GQ-to-duplex selectivity.<sup>25,53,54</sup> In our study, small-molecule ligands were designed by structural tuning of the carbazole core with various acceptor moieties and an aldehyde group to provide a higher selectivity to specific GQ targets *in cellulo*. We delineated the role of the aldehyde group in carbazole ligands to discriminate GQ topologies in *c-MYC* and *BCL-2* oncogenes.<sup>55,56</sup> In addition, these ligands inhibited rRNA biogenesis by displacing Nucleolin from multiple GQ-forming regions in the rDNA promoter, leading to the diminution of the enhanced protein synthesis of cancer cells.

Our study revealed dual-targeting GQ binding ligands that act like “double-edged swords” in synergistically arresting multiple oncogenic pathways.

## RESULTS AND DISCUSSION

### Design and Syntheses of Carbazole-Based Monocyanine Ligands

Carbazole-based compounds are widely used in medicinal chemistry because of their pleiotropic biological attributes (*i.e.*, anticancer, antifungal, antibacterial, antiviral, and anti-inflammatory) and appealing photophysical properties.<sup>57–60</sup> The carbazole core consists of a large aromatic system with a central nitrogen atom in the five-membered ring showing extensive electron delocalization, which could be harnessed with different electron acceptor moieties to construct electron donor– $\pi$ –electron acceptor (D– $\pi$ –A) organic dyes (Figure 1A). Furthermore, the rotation of D and A units around the double bond linker allows the carbazole ligands to adopt a flexible conformation, which can be restricted to optimize  $\pi$ – $\pi$  stacking upon interaction with the G-tetrads. Previous studies revealed that various pharmacomodulations in the tricyclic carbazoles contribute to their antitumor activities and selective recognition of topologically divergent GQ structures.<sup>61,62</sup> Thus, we designed and synthesized a series of carbazole-based monocyanines using Knoevenagel condensation as the key reaction step for conjugating carbazole di- or monoaldehyde with methylated benzothiazole (TCA and TCZ), lepidine (LCA and LCZ), and quinaldine (QCA and QCZ) scaffolds as the acceptor moieties to obtain D– $\pi$ –A-based ligands with extended  $\pi$ -conjugation (Figure 1B).<sup>63,64</sup> An ethyl substituent at the nitrogen atom was incorporated as it offers facile electron delocalization between D and A moieties enhancing the emission properties and providing enhanced nonpolar interactions upon GQ binding. Most of the designed aromatic ligands have a marked tendency to bind avidly and indiscriminately to GQ structures through large hydrophobic surfaces, while polar aldehyde groups offer critical hydrogen bonding for selective interactions. We measured the topological polar surface area (TPSA) using a reported methodology, which is defined as a sum of the surface area of nitrogen and oxygen plus hydrogen atoms attached to the heteroatoms. This phenomenon is known to correlate well with hydrogen bonding.<sup>65</sup> Indeed, the presence of the aldehyde group increased the molecular polar surface area by 3-fold (25.89 Å<sup>2</sup>) compared to the carbazole derivatives without the aldehyde group (8.82 Å<sup>2</sup>), as shown in Table S3. To check their differential binding with various GQ structures, several oncogene GQs (*c-MYC*, *BCL-2*, *VEGF-A*, and *KRAS*) had been used that harbor dynamic conformational ensembles of GQs in cellular milieu for their normal functions.<sup>66,67</sup> Since the fluorescence property of carbazole is highly sensitive to the macromolecular crowding of the cellular microenvironment,<sup>68</sup> different acceptor moieties were introduced to tune their electronic properties for the desired turn-on emission upon GQ binding.<sup>69</sup> We investigated the structure–activity relationships of the carbazole ligands to understand the role of different acceptor moieties and the aldehyde group present in TCA/LCA/QCA for their potential on differential GQ selectivity (or optical response) in the cells.

### In Vitro GQ Selectivity of Carbazole-Based Monocyanine Ligands

The judicious design and conjugation of the carbazole unit with benzothiazole, lepidine, or quinaldine to construct D– $\pi$ –A ligands (TCA/TCZ, LCA/LCZ, and QCA/QCZ) led to excitation and emission wavelengths of the resulting ligands in the visible region, an essential prerequisite to avoid autofluorescence and photodamage during cellular imaging. The photophysical properties of all the derivatives were measured in solvents of different polarities, *viz.*, dichloromethane (DCM), tetrahydrofuran (THF), dimethyl sulfoxide (DMSO), and phosphate buffered saline (PBS) buffer to understand the solvatochromic effects (Figure S1). Their absorption and emission intensities were gradually enhanced accompanied by the bathochromic and hypsochromic shifts, respectively, with the decrease in solvent polarity (PBS to DCM). This observation revealed that the photophysical properties of carbazole derivatives are sensitive to polarity and exhibit positive solvatochromism in the organic solvents (DCM, THF, and DMSO). The observed solvatochromic effects indicated the sensitivity of carbazole derivatives to the microenvironment offered by any target. These carbazole compounds showed broad and featureless absorption bands around 435–450 nm ( $\lambda_{\max}^{\text{abs}}$ ) in 20 mM PBS, 100 mM KCl, pH 7.4, at 24 °C (Table S3 and Figure S3). TCA, LCA, and QCA showed a large bathochromic shift ( $\lambda_{\max}^{\text{abs}} = 20$ –45 nm) in the presence of GQ DNA compared to that of the duplex DNA ( $\lambda_{\max}^{\text{abs}} = 2$ –10 nm) (Table S3 and Figure S3). While the hyperchromic effect was observed in the absorption spectrum of TCA in the presence of GQ, the rest of the ligands (LCA, QCA, TCZ, LCZ, and QCZ) exhibited a differential hypochromic effect in the presence of GQ. TCZ, LCZ, and QCZ exhibited a moderate increase in the bathochromic shift ( $\lambda_{\max}^{\text{abs}} = 15$ –30 nm) for GQ DNA compared to duplex DNA ( $\lambda_{\max}^{\text{abs}} = 10$ –15 nm) with a concomitant decrease in their absorptivities (Table S3 and Figure S3). The hypochromic effect and moderate to large bathochromic shifts of the absorption maximum were characteristic of  $\pi$ -stacking interactions between the ligand and GQ.<sup>70</sup> This finding suggested that the carbazole ligands possess an appropriate planar core size for  $\pi$ -stacking interactions with the external G-tetrad surface. These ligands exhibited a very weak fluorescence ( $\lambda_{\max}^{\text{em}}$ ) around 550–610 nm in PBS buffer (Table S3 and Figure S4). Upon gradual titration of different promoter GQs (*TEL22*, *c-MYC*, *BCL-2*, *VEGF-A*, *c-KIT*, and *KRAS*), a strong and progressive turn-on fluorescence response (up to 5–10-fold for TCA/LCA/QCA (Figure 2A,C) and 15–80-fold for TCZ/LCZ/QCZ (Figure 2D–F) was observed. The ligands showed a negligible fluorescence enhancement upon duplex titrations.<sup>71</sup> The fluorescence enhancement in the presence of GQs is attributed to the decreased polar environment and reduction in the nonradiative decay of the photoexcited monocyanines due to the restricted rotation of A and D moieties around the central C=C bond upon GQ binding. This suggested that GQ topology provides a hydrophobic pocket for the binding interaction of carbazole ligands, which in turn prevents the fluorescence quenching by polar water molecules. Interestingly, these carbazole ligands exhibited large Stokes shifts between the absorption and emission spectra ( $\Delta\lambda = 130$ –160 nm) (Table S3), which helps to overcome the shortcomings of classic cyanine dyes that suffer from a narrow Stokes shift ( $\Delta\lambda < 25$  nm)-related self-quenching and measurement errors compromising the

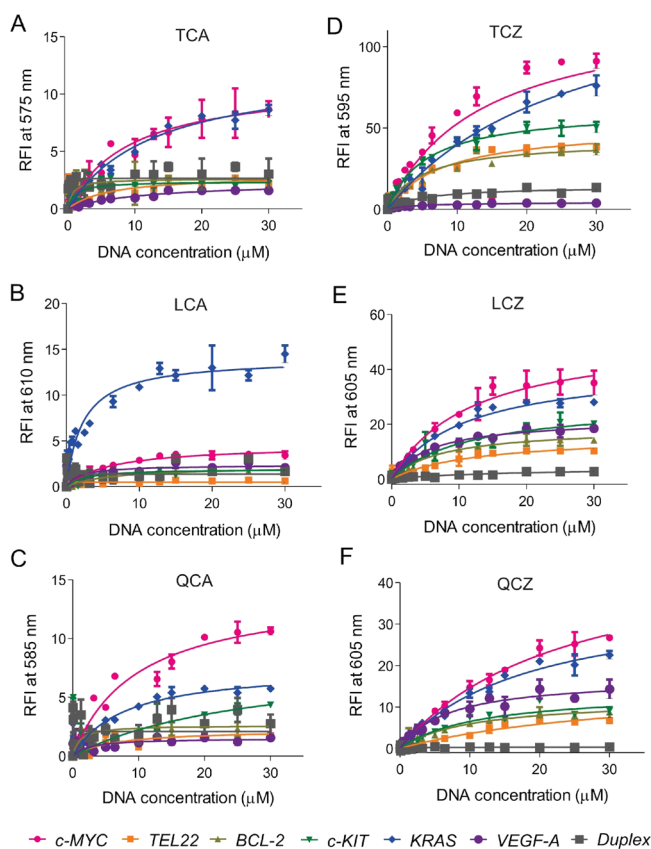


**Figure 2.** Selective recognition of GQ with turn-on fluorescence response of carbazole ligands. Relative fluorescence intensities (RFIs) of carbazole ligands (A) TCA, (B) LCA, (C) QCA, (D) TCZ, (E) LCZ, and (F) QCZ (5 μM) titrated with varying concentrations of GQ or duplex (0–30 μM) forming DNA sequences measured in phosphate buffer (20 mM PBS, 100 mM KCl, pH 7.4, at 24 °C). Error bars present mean ± SE ( $N = 3$ ).

detection sensitivity.<sup>72</sup> Nevertheless, the fluorescence emission of carbazoles may depend on many factors including the rigidity of ligands upon binding to GQ, which underscored that the binding constants and fluorescence response may not have a direct relationship.<sup>73</sup> Therefore, further investigations were performed to understand their differential binding modes with various GQ structures.

### Anticancer Activity of Carbazole Ligands

The antiproliferative effect of carbazole ligands was evaluated in different human cancer cell lines (MCF-7, MDAMB-231, T47D, and HeLa) and nontransformed (HEK293T) cells by the MTT (3-(4,5-dimethylthiazol-2-yl)-2,5-diphenyl tetrazolium bromide) assay (Table S4). After 24 h of treatment, TCZ/LCZ/QCZ showed better antiproliferative effects in the cancer cell lines than TCA/LCA/QCA. The carbazole ligands (TCA and TCZ) with a benzothiazolium acceptor moiety exhibited the lowest cytotoxic effects in normal cells while exhibiting significant antiproliferative effects in cancer cells at low micromolar concentrations. The lepidine and quinaldine derivatives (LCA and QCA, respectively) with the aldehyde group exerted less antiproliferative effects in cancer cells compared to that of the derivatives without the aldehyde group (LCZ and QCZ). Unlike the benzothiazolium derivatives, lepidine- and quinaldine-containing ligands showed a certain degree of toxicity in normal cells, which is possibly attributed to their off-target effects. Intriguingly, the cytotoxic effects of

TCA and TCZ were found significantly higher in MDAMB-231 and MCF-7 cells, wherein the overexpression of *c-MYC* and *BCL-2* contributes to the cancer cell survival and tumorigenicity.<sup>74–76</sup>

We performed a flow cytometry-based apoptosis detection assay to speculate the mode of antiproliferation by carbazole ligands. Cells were treated with carbazoles in a dose-dependent manner for 24 h, and Annexin V-FITC/PI dual staining was carried out for the quantitative assessment of live, early apoptotic, and necrotic or dead cell population (Figure 3A,B). Cells treated with 1 μM TCA and LCA showed ~30–46% early apoptotic cells at 24 h, which is 25-fold higher than that of the untreated cells. In contrast, treatment with QCA resulted in ~50% of cells in the late apoptotic or necrotic state. In congruence with the cytotoxicity data, TCZ/LCZ/QCZ derivatives were more potent to induce apoptosis at lower concentrations (500 nM) compared to that of the carbaldehyde (TCA/LCA/QCA) ligands. At 500 nM concentration of TCZ and LCZ, ~40–50% of the population was found to be in the early apoptosis stage, which is approximately 25-fold higher compared to the control. At 1 μM concentration, LCZ and QCZ treatment led to as much as ~90–95% of the population into the late apoptotic stage at 24 h. With these findings, TCA, LCA, and TCZ were observed to induce apoptosis in MDAMB-231 cells that might account for the observed antiproliferative effect. We also monitored the expression of apoptotic markers at the protein level (Figure 3C,D). Consistent with flow cytometric results, TCA/TCZ treatment significantly upregulated the cleavage of PARP (poly(ADP-ribose) polymerase) and caspase 3 and 9 (cysteine-aspartic proteases), while the *BCL-2* level is reduced, sensitizing the cancer cells to apoptotic death.

### Selective Targeting of *BCL-2* and *c-MYC* Promoter GQs by TCA and TCZ, Respectively

To evaluate the role of GQ-mediated transcription regulation in *c-MYC*, *BCL-2*, *KRAS*, and *VEGF-A* promoters that harbor GQ motifs, we performed dual-luciferase assays in MDAMB-231 cells, transfected with the reporter plasmids containing Renilla luciferase coding sequences downstream GQ scaffolds of the oncogenes of interest (Figure 4A). *c-MYC*, *BCL-2*, *VEGF-A*, and *KRAS* are involved in multiple crosstalk and cellular pathways leading to cellular growth and apoptosis regulation in MDAMB-231 and different cancer cells. *KRAS* and *VEGF* were found to directly influence the expression of *c-MYC* and *BCL-2* genes, being involved in their signaling pathways.<sup>77,78</sup> Further, their promoter GQs are structurally different in terms of sequence context, loop nature, groove dimensions, and the number of tetrads that might offer differential binding to the carbazole ligands, and all these GQs exhibit conformational ensemble and structural plasticity in the cellular milieu.<sup>6</sup> Therefore, we determined the promoter activity of these oncogenes (*c-MYC*, *BCL-2*, *VEGF-A*, and *KRAS*) under the treatment of carbazole ligands in a dose-dependent manner for 24 h in MDAMB-231 cells (Figure 4A–C and Figures S5 and S6). The constructs having GQ-deleted oncogene promoters were constitutively activated irrespective of carbazole ligand treatment, while the oncogene promoters having upstream GQ structures of distinct topologies manifested into differential luciferase activities, reflecting that the carbazole ligands triggered differential regulation of the oncogene promoters only in the presence of the upstream GQ motifs (Figure 4B,C and Figures S5 and S6). This finding

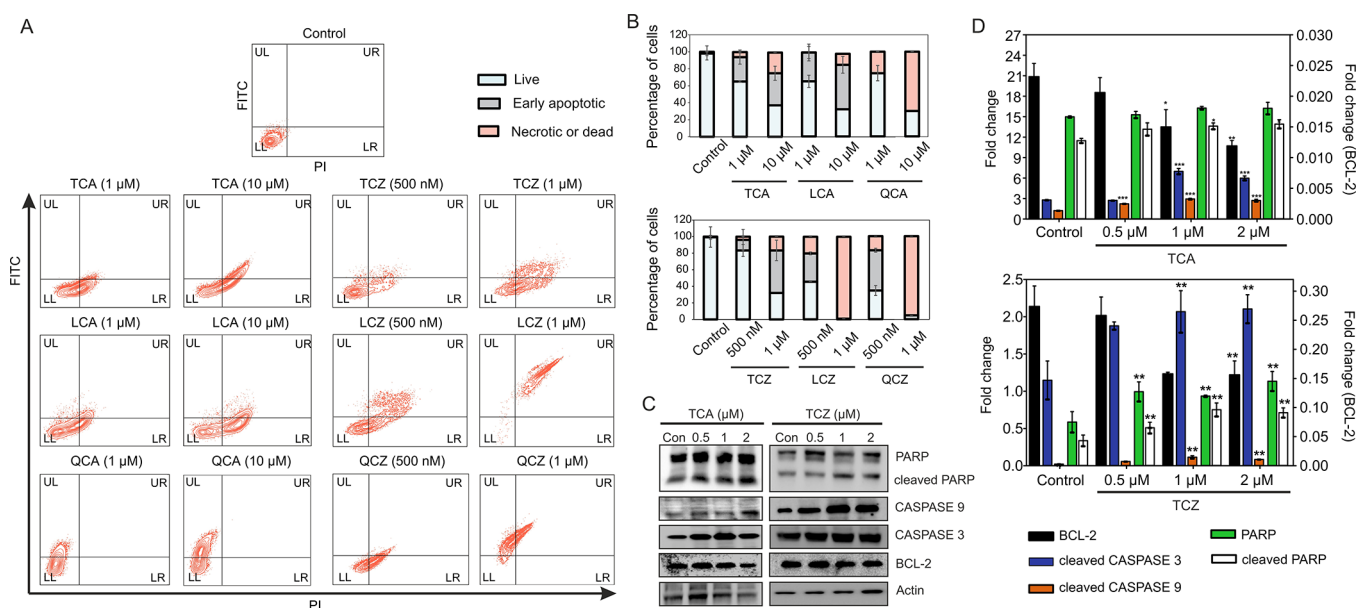


**Figure 3.** Apoptosis induction by carbazole ligands. (A) Flow cytometric analysis of an Annexin V-FITC/PI dual staining assay after treatment with TCA/LCA/QCA (1 and 10  $\mu\text{M}$ ) and TCZ/LCZ/QCZ (500 nM and 1  $\mu\text{M}$ ) for 24 h in MDAMB-231 cancer cells; LL, LR, UR, and UL indicate the live cells and early, late apoptotic, and necrotic cells, respectively. (B) Bar plots denote the estimation of live, early apoptotic, and necrotic or dead cells. FITC: fluorescein isothiocyanate and PI: propidium iodide. (C) Western blot images showing expression of different apoptotic markers under increasing concentrations of TCA and TCZ in MDAMB-231 cells at 24 h. Actin was used as the housekeeping protein. (D) Bar plots determine the fold change expression of apoptotic markers compared to the control based on densitometric analyses. Error bars present means  $\pm$  SE ( $N = 3$ ).

confirmed the superior GQ-to-duplex selectivity of carbazole ligand in cancer cells, which agrees with fluorescence spectroscopy data. The magnitude of GQ-driven promoter inhibition significantly varied in different oncogenes suggesting a differential binding mode of interaction. Although KRAS GQ exhibited considerable fluorescence enhancement upon binding to six compounds, we observed differential promoter regulation upon carbazole treatment *in cellulo*. The KRAS promoter is a repository of three adjacent long GQ-forming stretches, known as near, mid, and far GQ regions separated by 15 and 10 base pairs. Unlike the *in vitro* condition, wherein we used the near KRAS GQ sequence only, the cellular GQ structure is neighbored by two GQ motifs at a close proximity. This sequence organization within cellular conditions is anticipated to impact the folding kinetics and structural properties of the near GQ structure compared to that of the experimental conditions. The lepidine derivatives showed nonselective binding to GQ motifs at *c-MYC*, *BCL-2*, and *VEGF-A* promoters producing significant attenuation to their promoter activities (Figure S5), which suggested their inefficiency for selective targeting of GQ scaffolds *in cellulo*. At a higher concentration, LCA and LCZ arrested KRAS promoter activation, suggesting their weak interaction to its promoter quadruplex at a higher concentration in contrast to the observed selective fluorescence response.

The nonspecific GQ binding was further corroborated by the significant downregulation of *c-MYC*, *BCL-2*, *VEGF-A*, and *KRAS* transcription upon LCA and LCZ treatment (Figure 4D,E). Similarly, quinaldine ligands (QCA and QCZ) repressed the promoter activity and transcription of *BCL-2*, *c-MYC*, *KRAS*, and *VEGF-A* oncogenes bearing GQ structures, indicating their failure to discriminate different oncogenic quadruplex conformations in the cells (Figure S5 and Figure 4D,E). These findings envisaged that the cytotoxic effects of

lepidine and quinaldine ligands might have emanated from their nonspecific binding to various GQ topologies and associated off-target effects. On the contrary to the observed indiscriminate fluorescence response, benzothiazole derivatives (TCA and TCZ) showed no significant effect on KRAS and *VEGF-A* promoter regulation (Figure 4A,B). However, TCZ and TCA selectively reduced the promoter activation of *c-MYC* and *BCL-2* promoters, respectively, indicating their distinct interaction with specific oncogenic GQs in MDAMB-231 cells promoting low expression of the corresponding Renilla luciferase in a dose-dependent manner (Figure 4B,C and Figure S6). Although both of the GQ structures formed at *c-MYC* and *BCL-2* promoters feature single-nucleotide G3NG3 double-chain-reversal loop (N denotes any nucleotide) that contribute to their stability and facile reversibility, they exhibit structural differences in terms of sequence, groove dimensions, and the nature of other connecting loops.<sup>79</sup> The selectivity of TCA and TCZ toward GQs at *c-MYC* and *BCL-2* promoters possibly resulted from their potential to distinguish the structural properties of *c-MYC* and *BCL-2* GQs. However, we observed weak repression ( $\sim 1.25$  fold) of the *VEGF-A* promoter at 1  $\mu\text{M}$  TCZ treatment for 24 h, suggesting its weak interaction with the *VEGF-A* quadruplex in the cells at a higher concentration (Figure 4C). Nevertheless, TCZ at a low concentration (500 nM) reduced *c-MYC* promoter activity to a relatively greater extent ( $\sim 2$ -fold) compared to that of KRAS and *VEGF-A* promoters, suggesting a higher affinity of TCZ for *c-MYC* GQ compared to other oncogenic GQ motifs under the cellular microenvironment.

The GQ selectivity for target-specific oncogenes by TCA and TCZ impinged on the analyses of intermolecular interactions and thermodynamic binding interactions upon GQ association, which led us to investigate the thermodynamic parameters of their binding interactions to various oncogenic

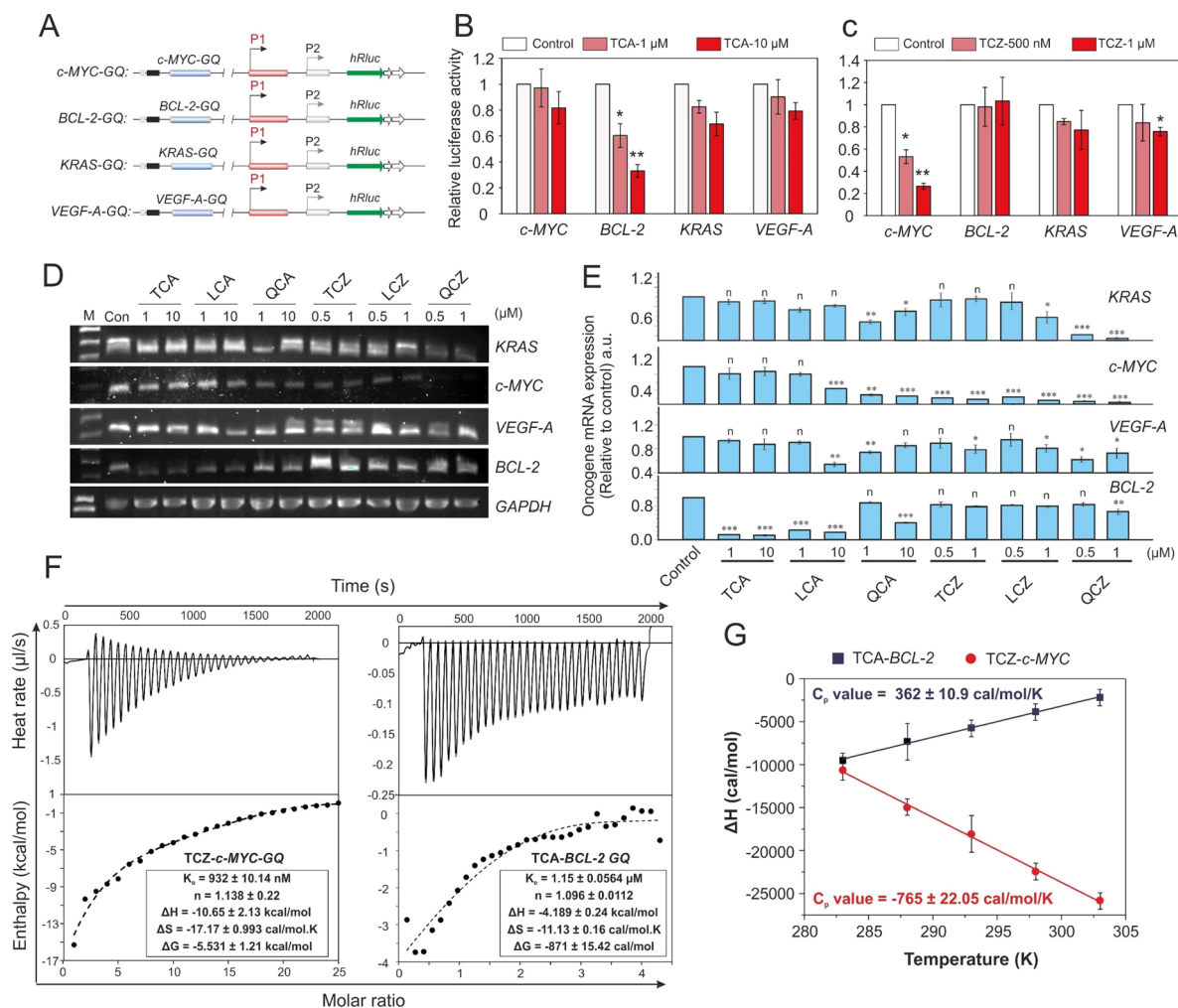


**Figure 4.** Selectivity of carbazole derivatives for different oncogenic GQs in MDAMB-231 cells. (A) Schematic diagrams of oncogene promoter sequences with upstream GQ-forming elements, cloned into a promoter-less pGL4.72[hRlucCP] luciferase vector. *hRluc*, Renilla luciferase gene; P1 and P2, promoters of oncogenes. Evaluation of *c-MYC*, *BCL-2*, *KRAS*, and *VEGF-A* promoter activities under 24 h of treatment of (B) TCA and (C) TCZ using the reporter plasmids with or without the respective wild-type GQ-forming sequences. Relative promoter activity determined by normalizing the Rluc/Fluc values to that of the cells transfected with oncogene promoter constructs (GQ-null), having no GQ-forming motif. Error bars represent mean  $\pm$  SE ( $N = 5$ ). (D) Semiquantitative RT-PCR analysis and (E) RT-PCR showing the expression profiles of *c-MYC*, *BCL-2*, *KRAS*, and *VEGF-A* transcription upon 24 h of treatment of TCA/LCA/QCA (1 and 10  $\mu$ M) and TCZ/LCZ/QCZ (500 nM and 1  $\mu$ M) in MDAMB-231 cancer cells. M, 100 bp ladder; Con, control. Quantification of the transcripts' level relative to the control (*GAPDH*). Error bars represent mean  $\pm$  SE ( $N = 3$ ). Statistical differences determined compared to the control by two-tailed Student's *t* test (\* $P < 0.05$ , \*\* $P < 0.01$ , \*\*\* $P < 0.001$ , *n*, statistically nonsignificant). (F) ITC binding profiles of TCZ and TCA with *c-MYC* and *BCL-2* promoter GQ sequences, respectively, in 10 mM potassium phosphate buffer (pH 7.0), 100 mM KCl at 25  $^{\circ}$ C. The solid line represents the best fit data using "one site binding model". (G) Temperature dependence of heat capacity changes ( $\Delta C_p$ ) at constant pressure measured for TCA-GQ or TCZ-GQ complex formation.

GQ motifs and telomeric GQ by ITC (Figure 4F, Figures S7 and S8, and Table S5). We slowly titrated the oncogenic GQ sequences into carbazole ligands at soluble concentrations (Figure S2) and analyzed the integrated heat release of the titrations to elucidate the thermodynamic partitioning of binding free energy ( $\Delta G$ ) between enthalpic and entropic components. Indeed, we witnessed a series of enthalpy-dominated exothermic binding reactions between benzothiazolium ligands and GQs, as the binding enthalpy ( $\Delta H$ ) overcompensated for the unfavorable loss in conformational entropy ( $\Delta S$ ). The magnitude of  $\Delta H$  was relatively more negative than  $\Delta S$ , hence contributing substantially to the binding free energies during the interactions. Despite the fact that TCA and TCZ showed a higher affinity for *BCL-2* and *c-MYC* GQs, respectively, the heat capacity change of binding

was found to be significantly different, suggesting differential mode of GQ binding by the ligands (Figure 4G). The heat capacity contribution ( $\Delta C_p$ ), calculated from the slope of  $\Delta H$  versus temperature for TCA-*BCL-2* GQ binding was positive, which might be caused by an increased thermal motion, resulting in a smaller change in entropy. The magnitude of TCA and *BCL-2* GQ interaction was greatest concerning water dipole, contributing a net positive heat capacity change in the binding reaction.<sup>80</sup> On the other hand, the  $\Delta C_p$  value of TCZ-*c-MYC* GQ was negative, which suggested the burial of the hydrophobic surface or the disruption of electrostatic interactions.<sup>81</sup> In agreement with the fluorescence data, the ITC study suggested that these compounds have no significant interactions with duplex DNA (Figure S20).

Molecular docking showed that TCZ binds to the groove of *c-MYC* GQ through a network of electrostatic, hydrogen bonding, and nonpolar interactions, providing a higher binding selectivity for *c-MYC* GQ (Figure S9 and Tables S6 and S7). This observation is supported by the earlier reports from Leung's group, which revealed that the binding in the grooves and loops of *c-MYC* GQ can potentially offer a higher degree of selectivity.<sup>24,82</sup> In contrast, TCA prevalently exhibited stacking interaction at the proximity of 5'-end of *BCL-2* GQ (Figure S9A), where carbazole and benzothiazolium moieties were involved in a multitude of nonpolar and electrostatic interactions, rendering the GQ stability (Figure S10 and Table S8). We have further performed a 50 ns simulation of the docked complexes in explicit solvent that provided further weightage to their mode of interactions (Figure S22A,C). The average RMSDs (root-mean-square deviations) of TCA and TCZ are in a range of 1.2–1.5 Å, which underlines that TCA preferred the stacking interaction while TCZ binds to the groove in the respective GQs. To further support these results, NMR titration was performed on TCZ/TCA in the presence or absence of *c-MYC* or *BCL-2* GQs, respectively (Figure S11). Consistent with the docking studies, we observed the upfield shifts of H15, H17, and H23 in a TCA carbazole moiety upon *BCL-2*-GQ titration, suggesting the shielding of the carbazole ring due to  $\pi$ -stacking interactions with *BCL-2* GQ. The line-broadening of proton resonances in both carbazole and benzothiazolium moieties of TCA provided further evidence for other noncovalent interactions between TCA and *BCL-2* GQ. An upfield shift of the H28 proton indicated hydrogen bond formation between the aldehyde group and G16, which seemed to strengthen the  $\pi$ - $\pi$  stacking between the carbazole ring and *BCL-2* GQ (Table S6). In contrast, we did not find a strong stacking between the TCZ carbazole aromatic ring and *c-MYC* GQ. Instead, multiple splitting of H20, H15, and H19 of the TCZ carbazole ring was observed upon *c-MYC*-GQ titration, which might have emanated from two distinct states of free and bound TCZ with minor conformational differences at the proximity of the binding pocket. Therefore, the aldehyde group presumably allowed a favorable position of the carbazole core to facilitate  $\pi$ - $\pi$  stacking with GQs. In agreement with the docking studies, we further observed line-broadening of H1, H2, H3, and H6 of TCZ that indicated the prevalence of noncovalent interactions between the benzothiazolium moiety of TCZ and *c-MYC* GQ in the loop region. Interestingly, we found peak multiplicity and different coupling constants for H25 and H26 in both TCA and TCZ upon GQ titration, which indicated the restricted rotation of their central C=C bond upon GQ interactions. The differences in GQ interaction by TCA and TCZ were also reflected in the entropy–enthalpy compensation and different free energy changes during binding reactions. Therefore, by introducing the benzothiazolium moiety and/or aldehyde group in the lead carbazole molecules, we obtained selectivity gains for structurally different GQs with different thermodynamic signatures. In particular, we showed that strong enthalpic interactions improved selectivity for GQs even if they did not confer major changes in GQ binding affinity. This finding directly addressed the issue of improving GQ selectivity for modified carbazoles that already exhibited high GQ binding affinity. Our study provided a useful roadmap for the optimization of carbazole compounds to achieve a higher selectivity for structurally and functionally related GQ structures in the oncogenes.

### Role of TCA and TCZ in Regulating the GQ-Mediated Transcription of *c-MYC* and *BCL-2*

To gain a deeper insight into the role of benzothiazolium ligands (TCA/TCZ) in the GQ-driven transcription of *c-MYC* and *BCL-2*, we evaluated the displacement of transcription factors at the nuclease hypersensitive element (NHE) of *c-MYC* and *BCL-2* oncogenes by TCA/TCZ treatment. Earlier reports claim that Sp1 (Specificity protein 1) induces negative superhelicity at *c-MYC*-NHE III<sub>1</sub> to uplift the transcription.<sup>83</sup> Nucleoside diphosphate kinase (NM23-H2) unfolds *c-MYC* quadruplex to enhance the rate of transcription, while Nucleolin attenuates the promoter activation by stabilizing the quadruplex and outcompeting NM23-H2 occupancy.<sup>83–85</sup> In this study, we conducted ChIP studies on a region encompassing *c-MYC*-NHE III<sub>1</sub> and monitored the changes in promoter occupancy of Sp1, NM23-H2, and Nucleolin upon TCZ treatment (Figure 5A,B,E). We observed that TCZ strongly inhibits the abundance of Sp1 and NM23-H2 at *c-MYC*-NHE III<sub>1</sub>, which plays a central role in upregulating *c-MYC* transcription (Figure 5B,C). This accounted for its selective binding with *c-MYC* GQ under the cellular micro-environment and underscored the mechanism of its inverse effect in *c-MYC* transcription regulation. Surprisingly, treatment with 1  $\mu$ M TCZ did not show a significant change in Nucleolin recruitment at *c-MYC*-NHE III<sub>1</sub>, which might give synergistic stability to *c-MYC* GQ by displacing NM23-H2.

This result was further corroborated with the observation that the combined treatment of recombinant NM23-H2 (rhNM23-H2) and TCZ in MDAMB-231 cells significantly increased Nucleolin recruitment (Figure 5D). Neither could rhNM23-H2 treatment remarkably surpass Nucleolin occupancy in *c-MYC*-NHE III<sub>1</sub> in the presence of TCZ albeit having a strong antagonism with Nucleolin binding at the quadruplex element (Figure 5D).<sup>86</sup> On the other hand, NM23-H2 occupancy at *c-MYC* GQ had been strongly decreased by TCZ treatment. siRNA-knockdown of Nucleolin combined with TCZ treatment could not significantly restore the NM23-H2 enrichment at *c-MYC* GQ, indicating the plausible mechanism of *c-MYC* transcription inhibition by TCZ treatment (Figure 5E). Earlier reports claimed that WT1 (Wilm's tumor 1) positively regulate *BCL-2* transcription and binds to its NHE region containing the GQ forming motif.<sup>87,88</sup> In this study, we showed that TCA downregulated the recruitment of WT1 in the *BCL-2* promoter, which leads to  $\sim$ 2-fold depletion in *BCL-2* transcription in MDAMB-231 cells compared to that of the control (Figure 5F–H). Taken together, ChIP data pointed to the GQ-dependent mechanism of inhibition by the lead compounds.

### GQ Visualization Using TCA and TCZ

The confocal images showing colocalization with DAPI (4',6-diamidino-2-phenylindole) revealed the localization of TCA/TCZ into a nuclear compartment after 1 h of incubation, which confirmed their binding to the oncogenic GQ structures (Figure 6). Furthermore, their colocalization with Nucleolin, a protein marker specific to the nucleolus, evidently showed nucleolar localization of TCA and TCZ (Figure 6A and Figure S12). To evaluate the binding of carbazole ligands (TCA and TCZ) to GQs in MDAMB-231 cells, immunofluorescence experiments were performed by employing highly specific GQ antibody BG4 to compare the localization of BG4 with TCA and TCZ. As shown in Figure 6B, TCA and TCZ foci significantly colocalized with BG4 staining in the nuclei, which

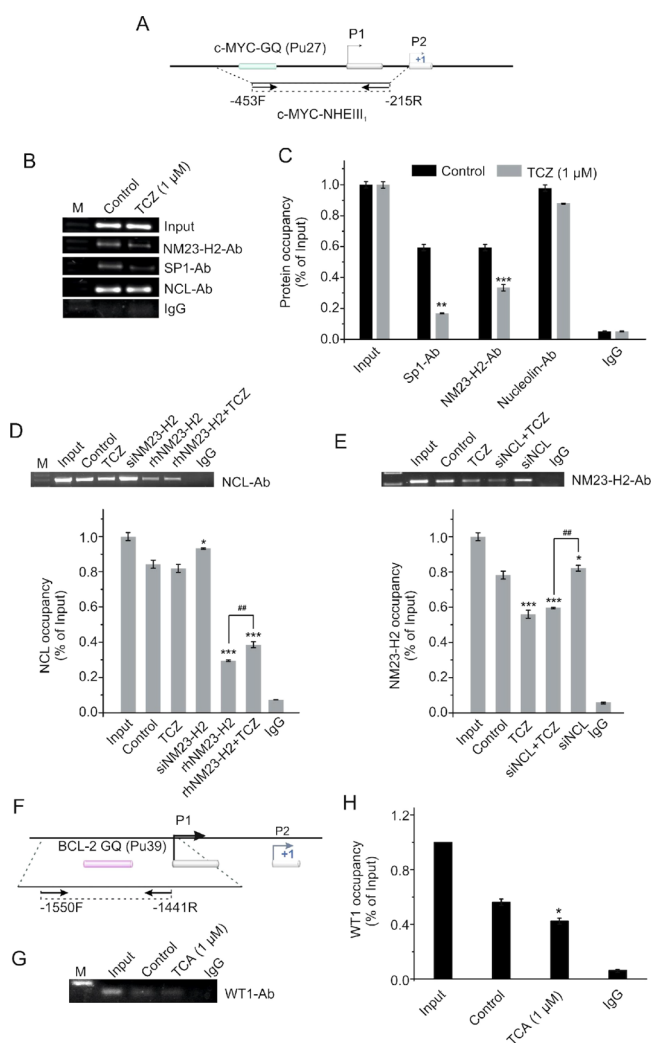


**Figure 5.** Role of TCA and TCZ to regulate GQ-mediated transcription of *BCL-2* and *c-MYC*. (A) Schematic of the *c-MYC* promoter with the GQ-forming region (Pu27) in the NHE III<sub>1</sub> region. ChIP primers were designed at the  $-453\text{F}$  to  $-215\text{R}$  region. F, forward and R, reverse primers. (B) ChIP experiments using NM23-H2-, Sp1-, and Nucleolin (NCL)-specific antibodies to evaluate their occupancy at the *c-MYC* promoter in MDAMB-231 cells under 1  $\mu\text{M}$  TCZ treatment for 24 h. The input fraction indicates total DNA; negative control immunoprecipitation uses rabbit IgG showing no signal. (C) Quantification of Sp1, NCL, and NM23-H2 occupancy at the *c-MYC* promoter by the percentage of the input method based on quantitative real-time PCR under 1  $\mu\text{M}$  TCZ treatment. (D) ChIP experiments using NCL-specific antibodies and quantification of NCL occupancy at the *c-MYC* promoter in MDAMB-231 cells. rhNM23-H2, recombinant NM23-H2 treatment for 24 h. (E) ChIP experiments using NM23-H2-specific antibodies and quantification of NM23-H2 occupancy at the *c-MYC* promoter in MDAMB-231 cells. Statistical difference for with or without TCZ in rhNM23-H2- or siNCL-treated cells calculated by Student's *t* test. (## $P < 0.01$ ) (F) Schematic representation of the *BCL-2* promoter having GQ-forming motif (Pu39) upstream P<sub>1</sub> and P<sub>2</sub> promoters. Target-specific primers for ChIP experiments were designated at the  $-1550\text{F}$  to  $-1441\text{R}$  region. (G) ChIP experiments using WT1-specific antibodies to evaluate its occupancy at the *BCL-2* promoter in MDAMB-231 cells under 1  $\mu\text{M}$  TCA treatment for 24 h. (H) Quantification of WT1 at the *BCL-2* promoter by the percentage of the input method based on quantitative real-time PCR. Error bars represent mean  $\pm$  SE ( $N = 3$ ). Statistical experiments for ChIP studies were performed by a one-way ANOVA Tukey–Kramer test. (\* $P < 0.05$ , \*\* $P < 0.01$ , \*\*\* $P < 0.001$ ).

was observed in the 3D images (Figures S13 and S14). The sensitivity of TCA and TCZ to visualize GQs in live cells was further recognized by longer fluorescence decay times observed *in vitro*. The time-correlated single photon counting (TCSPC) system was used to measure the fluorescence lifetimes of TCA and TCZ in the presence of quadruplex (*BCL-2* and *c-MYC*) and duplex DNA sequences (Figure 6C). TCZ showed 11- and 9-fold longer fluorescence decay times in the presence of *c-MYC* (0.79 ns) and *BCL-2* (0.63 ns) quadruplex, respectively, compared to duplex DNA (0.07 ns), endorsing the fluorescence measurements observed in Figure 2 as well as visual photographs shown in Figure S15. The lifetime traces of TCA showed slightly shorter fluorescence decay times in the presence of both *c-MYC* (0.078 ns) and *BCL-2* (0.063 ns) GQs compared to TCZ, which signified a slightly lower efficiency in detection (Table S8). While the lifetime traces of TCA in the presence of duplex could not be measured due to negligible fluorescence emission, the fluorescence lifetime measurements of TCA and TCZ showed longer decay times in the presence of GQs, which are in corroboration with the photophysical studies (Figure 2 and Figure S15). The appreciable differences observed in fluorescence lifetime decay further made TCZ and TCA as the promising probes to visualize GQs in live cells using a fluorescence lifetime imaging (FLIM) technique. Having shown the high GQ-binding affinity of TCA and TCZ and their localization in nucleoli, we anticipated their influence on ribosome RNA biogenesis, possibly to disrupt the interaction of rDNA GQs with the Nucleolin protein.

### Regulation of Ribosome Biogenesis

Ribosome biogenesis occurs in the nucleoli controlled by multiple signaling pathways that converge on the RNA Polymerase I complex (Pol I).<sup>89,90</sup> Pol I is directly responsible for the transcription of rRNA genes to generate pre-rRNAs (47S rRNA and 45S rRNA) that are processed to mature rRNA molecules (28S rRNA, 18S rRNA, and 5.8S rRNA), the key building blocks of ribosomes. Inhibition of Pol I transcription and ribosome biogenesis represent a novel approach to selectively disrupt proliferation of cancer cells. Quarfloxin (or CX-3543), the only GQ interacting molecule that had reached phase II clinical trials, was shown to localize in the nucleolus and selectively inhibit Pol I transcription through the disruption of GQ–Nucleolin complexes.<sup>5</sup> Nucleolin, a multifunctional nucleolar protein, plays an important role in maintaining transcriptional elongation of rDNA by Pol I and is implicated in regulation of ribosome biogenesis.<sup>91</sup> We performed ChIP analysis on rDNA regions encompassing multiple GQ-forming regions ( $-2905$ ,  $+48$ ,  $+12,855$ , and  $+5605$ ) to monitor the occupancy of Nucleolin upon TCA/TCZ treatment (Figure 7). TCA treatment resulted in a complete dissociation of Nucleolin from all GQ motifs in the rDNA promoter ( $-2905$ ,  $+48$ ,  $+12,855$ , and  $+5605$ ), leading to the strong inhibition of their biogenesis (Figure 7C). Meanwhile, TCZ decreased the Nucleolin abundance on all GQ-motifs in the rDNA promoter except for  $-2905$ , in contrast to TCA. This data indicated the better competence of TCZ in disrupting Nucleolin/GQ complexes on rDNA, compared to that of TCA. This observation was further confirmed by ITC displacement studies, which showed the better efficacy of TCA ( $K_D = 227$  nM) than TCZ ( $K_D = 900$  nM) in displacing rDNA GQs from Nucleolin-bound conditions (Figure S16).



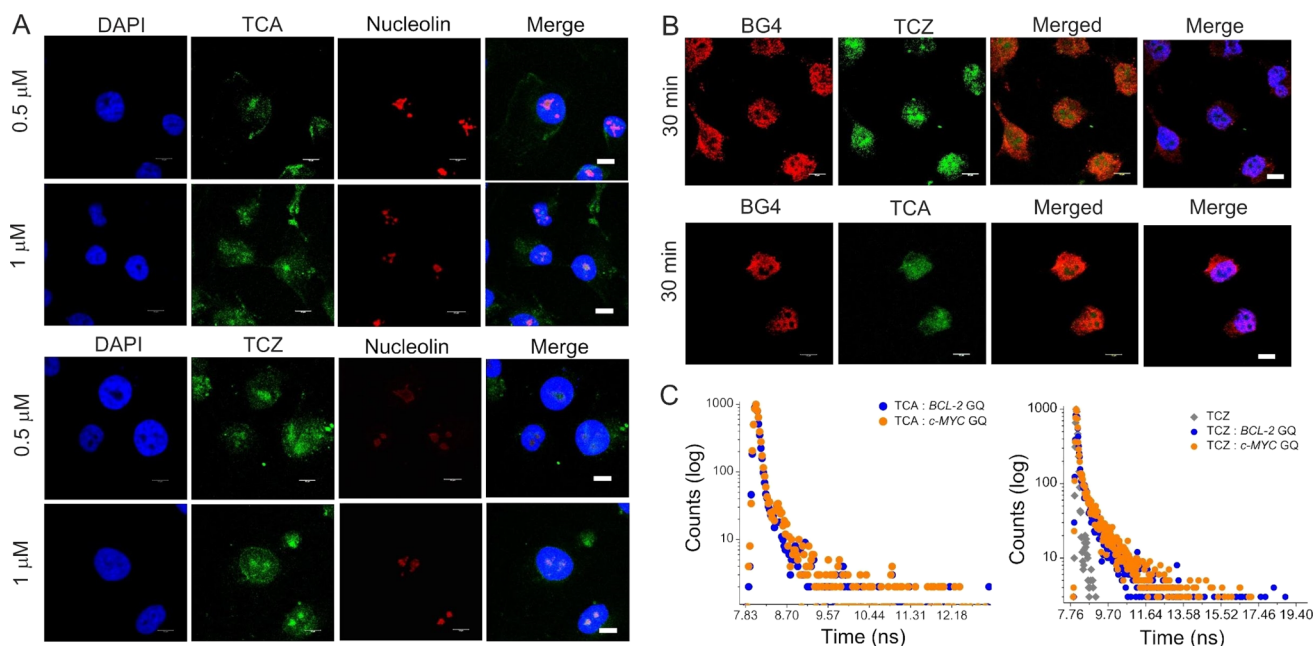


**Figure 6.** Cellular localization and lifetime decay of carbazole ligands. (A) Localization of TCA and TCZ (green) at different concentrations (0.5 and 1  $\mu\text{M}$ ) in MDAMB-231 cells by colocalizing with the Alexa 647-conjugated Nucleolin (red) antibody at 1 h timepoint. (B) Confocal images showing colocalization of TCA and TCZ (0.5  $\mu\text{M}$ ; green) with GQ selective antibody BG4 (red). Nuclei were stained with DAPI (blue). Scale bar: 10  $\mu\text{m}$ . (C) Fluorescence lifetime decay profiles of TCA and TCZ in the presence of GQ and duplex DNA at a 1:5 stoichiometric ratio.

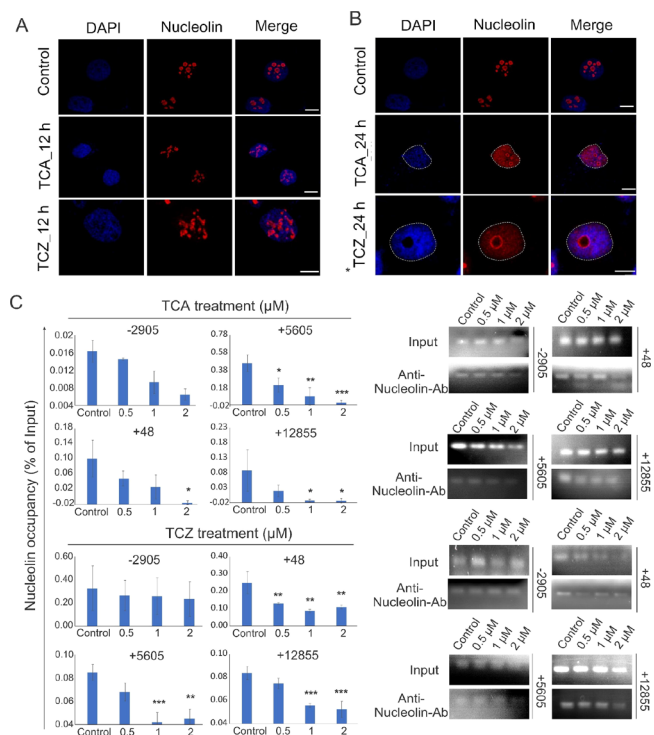


**Figure 7.** Ribosome biogenesis inhibition in MDAMB-231 cells. Confocal images showing (A) Nucleolin distortion and (B) nucleolar displacement upon treatment with TCA/TCZ (1  $\mu\text{M}$ ) at 12 and 24 h. Scale bar: 10  $\mu\text{m}$ . (C) ChIP results using Nucleolin-specific antibodies. Quantification of Nucleolin occupancy (% of input) at different rDNA regions (-2905, +5605, +48, and +12855) upon treatment with increasing concentration of TCA and TCZ for 12 h. Error bars represent mean  $\pm$  SE ( $N = 3$ ).

These results were further supported by the confocal images showing the translocation of Nucleolin from nucleolus to

nucleoplasm upon treatment with TCA/TCZ (Figure 7B) followed by an altered nucleolar architecture wherein Nucleolus appeared distorted at early time points (Figure 7A and Figure S12). The aberrant Nucleolin translocation and distortion signified compromised nucleolar integrity, an essential element for transcription of rDNA and ribosomal biogenesis. The nucleoli to nucleoplasm shuttle of Nucleolin might be one of the plausible underlying mechanisms that concentrated the occupancy of Nucleolin at *c-MYC* GQ upon TCZ treatment (Figure 5D) and significantly restored Nucleolin occupancy during combined treatment of recombinant NM23-H2 and TCZ. We further investigated the expression profiles of the genes involved in ribosomal biogenesis, *viz.*, 28S rRNA, 18S rRNA, 5.8S rRNA, and 47S and 45S precursor rRNAs. The levels of these rRNAs at 12 h time points were analyzed upon treatment with TCA/TCZ (Figure S17). RT-PCR data clearly showed the downregulation of 47S rRNA and 45S rRNA at 12 h, respectively, upon TCA treatment. The repression of 47S rRNA expression in the presence of TCZ at 12 h affected the subsequent transcription of 18S and 5.8S rRNA. Downregulation of these ribosomal genes by TCA and TCZ, mediated by inhibition of Pol I transcription, clearly impeded the ribosomal biogenesis and essential protein synthesis. However, the inhibition of rRNA biogenesis was more pronounced in TCA, compared to TCZ, which was consistent with the observation that TCA was more efficient to block the occupancy of Nucleolin at the rDNA promoter than that of TCZ. These findings envisaged the crux relationship between carbazole-induced impairment of rRNA biogenesis and the inhibition of *c-MYC* transcription, which relies upon the redistribution of Nucleolin into the nucleoplasm, leading to the synergistic effect in GQ stabilization at the *c-MYC* promoter.

## CONCLUSIONS

Selective targeting of GQs using small molecules aims to enhance intracellular GQ affinity and modulation of oncogenic functions with minimal off-target effects in cancer cells. In this study, we designed a set of small molecule ligands by conjugating different acceptor (benzothiazole, lepidine, and quinaldine) moieties with a carbazole (donor) moiety with/without an aldehyde group. These compounds showed a turn-on fluorescence response and longer fluorescence decay time upon GQ binding with excellent GQ-to-duplex selectivity that allowed them to visualize GQ dynamics in live cells. NMR titrations and ITC studies evidenced the contributions of distinct polar and nonpolar interactions between carbazole derivatives and oncogenic GQs, resulting in differential thermodynamic signatures. While TCZ conferred selectivity to *c-MYC* GQ through a network of hydrogen bonds and noncovalent interactions in the GQ groove, TCA provided selectivity toward *BCL-2* GQ through both  $\pi$ -stacking interactions with G-tetrad and noncovalent interactions in the loops. This differential magnitude in GQ selectivity was achieved by optimizing the lead carbazole ligands with various functional moieties. This study made the foundation for the lead optimization of carbazole ligands to improve their potential to discriminate structurally and functionally related cellular GQs. These varying functionalities in carbazole ligands were derived from the structure–activity relationships based on their GQ binding affinity and other related parameters (e.g., cytotoxicity and potential to inhibit GQ-mediated oncogenic transcription). Dual-luciferase assays provided a rapid read-out of their ability to discriminate endogenous GQs at oncogene promoters. We observed that lepidine (LCA/LCZ) and quinaldine (QCA/QCZ) conjugates were nonspecifically targeted at oncogenic GQs, resulting in transcriptional repression of all oncogenes bearing GQs. However, consistent with the *in vitro* studies, TCA and TCZ (benzothiazole conjugates) selectively suppressed the promoter activity and transcription of *BCL-2* and *c-MYC*, respectively, through GQ interactions upstream their promoter regions. Further investigations underscored the mechanism of action of TCZ and TCA in transcription inhibition, which relied on the displacement of GQ binding proteins (e.g., NM23-H2 and Sp1 in *c-MYC*; WT1 in *BCL-2*) from *c-MYC* and *BCL-2* promoters. The key finding of this work is focused on the lead optimization of carbazole ligands by structure–activity relationship to attain a higher selectivity to oncogenic GQs and reduced off-target effects for therapeutic intervention.

Besides the selective modulation of oncogenic function by TCA/TCZ, they were transported to the nucleolus and were found to dissociate Nucleolin/GQ complexes on rDNA and perturb ribosomal biogenesis. Our results revealed that TCA/TCZ displaces Nucleolin from GQ-motifs on the rDNA promoter, leading to the translocation of Nucleolin from nucleolus to the nucleoplasm and nucleolar distortion. This mechanism might further restore Nucleolin deposition at *c-MYC* GQ in the nucleoplasm adding bona fide stability to the quadruplex and *c-MYC* transcription attenuation. TCA/TCZ-induced nucleolar stress also impaired the synthesis of rRNA genes involved in ribosome biogenesis, implicating the synergistic effect in the diminution of translation competence of cancer cells arresting uncontrolled proliferation. Due to the growing tendency of sculpting the drugs against multiple cellular targets for the treatment of complex diseases like

cancer, we propose that dual action of carbazole ligands inhibit ribosomal biogenesis as well as the overexpression of *c-MYC* and *BCL-2* in the cancer cells, which play a pivotal role in sensitizing the cells to apoptotic death. These synergistic effects of carbazole ligands in dual repression of oncogene function and ribosome biogenesis hold tremendous potential to ameliorate the therapeutic goal.<sup>92</sup> These findings suggested the future scopes for dual-targeting strategy for GQ-based ligands that converge to apoptotic signaling in cancer cells.

## MATERIALS AND METHODS

### Chemistry

All compounds were purified to >95% as determined by analytical HPLC as well as <sup>1</sup>H- and <sup>13</sup>C-NMR and HRMS. The general chemistry and experimental information are supplied in the [Supporting Information](#).

### Synthetic Procedure

**Synthesis of 9-Ethyl-carbazole-3,6-dicarbaldehyde (1).** Dimethylformamide (DMF, 22 mL, 0.3 mol) was added slowly to POCl<sub>3</sub> (28 mL, 0.3 mol) under stirring conditions in an ice bath. After 30 min, a white precipitate was obtained and a solution of 1.5 g of 9-ethylcarbazole (16 mmol) in 20 mL of DMF was added. The mixture was slowly heated to 373 K and maintained at this temperature for 30 h and then cooled to room temperature. The brown viscous oily residue was poured into a mixture of ice-water followed by extraction with dichloromethane (DCM) (100 mL). The DCM layer was washed three times with water (100 mL) and dried over anhydrous magnesium sulfate. The solvent was evaporated under reduced pressure, and the residue was purified by silica-gel column chromatography using DCM:MeOH (100:0 to 99:1) as an eluant to obtain compound **1** in 50% yield.

**Synthesis of 9-Ethyl-carbazole-3-carbaldehyde (2).** DMF (15 mL) was added slowly to POCl<sub>3</sub> (15.2 g, 0.1 mol) under stirring conditions in an ice bath at room temperature until the solution turned red. Then, 9-ethylcarbazole (1.5 g, 16 mmol) dissolved in 25 mL of 1,2-dichloroethane was added. The mixture was heated to 353 K and maintained at this temperature for 8 h and cooled to room temperature. The reaction mixture was poured into a mixture of ice-water followed by extraction with DCM (100 mL). The DCM layer was washed three times with 100 mL of water and dried over anhydrous magnesium sulfate. The solvent was evaporated under reduced pressure, and the residue was purified by silica-gel column chromatography to obtain compound **2** with 50% yield.

**Synthesis of Carbazole-Based Monocyanine Ligands (TCA, LCA, QCA, TCZ, LCZ, and QCZ).** The synthesis of various carbazole-based monocyanine ligands was performed by the Knoevenagel condensation reaction of 9-ethyl-carbazole-3,6-dicarbaldehyde (**1**) and 9-ethyl-carbazole-3-carbaldehyde (**2**) with the corresponding 4-methylbenzothiazole, 4-methyllepidinium, or 4-methylquinolinium halide.<sup>93</sup> Alkylation of benzothiazole, lepidine, and quinaldine was carried out in a sealed tube in toluene with methyl iodide to yield the corresponding iodide salts **3–5** in high yield ([Scheme S2](#)). The Knoevenagel condensation of aldehydes **1** and **2** with the corresponding 4-methylbenzothiazole (**3**), 4-methyllepidinium (**4**), or 4-ethylquinolinium (**5**) iodide was carried out in the presence of catalytic amount of piperidine in a 1:1 mixture of dichloromethane and methanol to obtain carbazole-based monocyanine ligands (*E*)-2-(2-(9-ethyl-6-formyl-9*H*-carbazol-3-yl)vinyl)-3-methylbenzo[*d*]-thiazol-3-ium (TCA), (*E*)-4-(2-(9-ethyl-6-formyl-9*H*-carbazol-3-yl)-vinyl)-1-methylquinolin-1-ium (LCA), (*E*)-2-(2-(9-ethyl-6-formyl-9*H*-carbazol-3-yl)vinyl)-1-methylquinolin-1-ium (QCA), (*E*)-2-(2-(9-ethyl-9*H*-carbazol-3-yl)vinyl)-3-methylbenzo[*d*]thiazol-3-ium (TCZ), (*E*)-4-(2-(9-ethyl-9*H*-carbazol-3-yl)vinyl)-1-methylquinolin-1-ium (LCZ), and (*E*)-2-(2-(9-ethyl-9*H*-carbazol-3-yl)vinyl)-1-methylquinolin-1-ium (QCZ) in a moderate yield (56–62%), which were thoroughly characterized by <sup>1</sup>H-NMR, <sup>13</sup>C-NMR, and HRMS

techniques. TCA and TCZ were obtained at a purity >98% as determined by HPLC (data provided in the Supporting Information).

### Characterization Data

TCA:  $^1\text{H}$  NMR (400 MHz,  $\text{DMSO}-d_6$ ):  $\delta_{\text{H}}$  (ppm) 10.13 (s, 1H), 9.11 (s, 1H), 8.80 (s, 1H), 8.44–8.40 (t,  $J = 8.0$ , 2H), 8.26–8.23 (t,  $J = 8.4$ , 2H), 8.12–8.08 (m, 2H), 7.93–7.80 (m, 3H), 7.78–7.77 (d,  $J = 7.2$ , 1H), 4.63–4.57 (q,  $J = 7.2$ , 2H), 4.39 (s, 3H), 1.41–1.38 (t,  $J = 7.0$ , 3H).  $^{13}\text{C}$  NMR (100 MHz,  $\text{DMSO}-d_6$ ):  $\delta_{\text{C}}$  (ppm) 191.9, 171.9, 149.9, 143.9, 142.9, 141.9, 129.3, 129.2, 128.4, 128.2, 127.5, 126.4, 124.1, 123.3, 123.1, 123.0, 122.5, 116.6, 111.1, 110.8, 110.5, 37.9, 36.2, 13.8. HRMS (ESI-TOF,  $[\text{M}]^+$ ): calcd. 397.1369 for  $\text{C}_{25}\text{H}_{21}\text{N}_2\text{O}_5^+$ , found 397.1366.

LCA:  $^1\text{H}$  NMR (400 MHz,  $\text{DMSO}-d_6$ ):  $\delta_{\text{H}}$  (ppm) 10.1 (s, 1H), 9.29 (d,  $J = 6.4$ , 1H), 9.09 (d,  $J = 8.4$ , 1H), 9.03 (s, 1H), 8.81 (s, 1H), 8.48 (d,  $J = 8.0$ , 1H), 8.4 (d,  $J = 8.0$ , 1H), 8.37 (s, 3H), 8.26 (t,  $J = 8$ , 1H), 8.12 (d,  $J = 8$ , 1H), 8.05 (d,  $J = 8$ , 1H), 7.83 (q,  $J = 5.3$ , 2H), 4.55 (t,  $J = 7.2$ , 2H), 4.513 (s, 3H), 1.38 (t,  $J = 7.0$ , 3H);  $^{13}\text{C}$  NMR (100 MHz,  $\text{DMSO}-d_6$ ):  $\delta_{\text{C}}$  (ppm) 191.9, 152.8, 147.7, 144.1, 143.8, 142.0138.8, 134.9, 129.1, 128.9, 128.8, 127.9, 126.4, 126.2, 123.5, 123.1, 122.6, 121.7, 119.3, 117.1, 115.4, 110.5, 110.3, 44.6, 37.8, 13.8. HRMS (ESI-TOF,  $[\text{M}]^+$ ): calcd. 391.1798 for  $\text{C}_{27}\text{H}_{23}\text{N}_2\text{O}^+$ , found 391.1792.

QCA:  $^1\text{H}$  NMR (400 MHz,  $\text{DMSO}-d_6$ ):  $\delta_{\text{H}}$  (ppm) 10.15 (s, 1H), 9.02 (s, 1H), 8.99 (d,  $J = 8.4$ , 1H), 8.82 (s, 1H), 8.62 (d,  $J = 9.2$ , 1H), 8.54 (d,  $J = 9.2$ , 1H), 8.46 (d,  $J = 15.6$ , 1H), 8.31 (d,  $J = 8$ , 1H), 8.18–8.12 (m, 2H), 8.08 (d,  $J = 8.4$ , 1H), 8.00 (d,  $J = 15.6$ , 1H), 7.92 (t,  $J = 7.6$ , 1H), 7.87 (d,  $J = 8.4$ , 2H), 4.6 (s, 3H), 4.57 (q,  $J = 8$ , 1H), 1.39 (t,  $J = 7.2$ , 3H);  $^{13}\text{C}$  NMR (100 MHz,  $\text{DMSO}-d_6$ ):  $\delta_{\text{C}}$  (ppm) 191.9, 156.3, 148.4, 143.9, 143.4, 142.4, 139.2, 134.7, 129.9, 129.1, 128.7, 128.1, 127.5, 127.3, 123.3, 123.1, 122.5, 122.2, 120.7, 119.2, 116.5, 110.6, 110.3, 37.8, 13.8. HRMS (ESI-TOF,  $[\text{M}]^+$ ): calcd. 391.1798 for  $\text{C}_{27}\text{H}_{23}\text{N}_2\text{O}^+$ , found 391.1798.

TCZ:  $^1\text{H}$  NMR (400 MHz,  $\text{DMSO}-d_6$ ):  $\delta_{\text{H}}$  (ppm) 8.9 (s, 1H), 8.31 (dd,  $J = 4$ , 2H), 8.19–8.23 (m, 3H), 8.03 (d,  $J = 15.6$ , 1H), 7.71–7.87 (m, 4H), 7.56 (t,  $J = 7.4$ , 1H), 7.35 (t,  $J = 7.4$ , 1H), 4.54 (q,  $J = 7.2$ , 2H), 4.37 (s, 3H), 1.37 (t,  $J = 7.2$ , 3H);  $^{13}\text{C}$  NMR (100 MHz,  $\text{DMSO}-d_6$ ):  $\delta_{\text{C}}$  (ppm) 171.9, 150.6, 142.2, 141.9, 140.3, 129.1, 128.1, 127.9, 127.3, 126.8, 125.2, 124.0, 123.7, 122.9, 122.2, 120.6, 120.3, 116.5, 110.1, 37.4, 36.1, 13.8; HRMS (ESI-TOF,  $[\text{M}]^+$ ): calcd. 369.1420 for  $\text{C}_{24}\text{H}_{21}\text{N}_2\text{S}^+$ , found 369.1426.

LCZ:  $^1\text{H}$  NMR (400 MHz,  $\text{DMSO}-d_6$ ):  $\delta_{\text{H}}$  (ppm) 8.9 (d,  $J = 8$ , 1H), 8.8 (s, 1H), 8.6 (d,  $J = 8.0$ , 1H), 8.50 (t,  $J = 14$ , 2H), 8.28 (dd,  $J = 8.0$ , 2H), 8.17–8.11 (m, 2H), 7.96 (s, 1H), 7.92 (t,  $J = 7.4$ , 1H), 7.78 (d,  $J = 8.0$ , 1H), 7.70 (d,  $J = 8.0$ , 1H), 7.55 (t,  $J = 7.6$ , 1H), 7.33 (t,  $J = 7.4$ , 1H), 4.5 (s, 3H), 4.51 (q,  $J = 8$ , 2H), 1.37 (t,  $J = 8$ , 3H);  $^{13}\text{C}$  NMR (100 MHz,  $\text{DMSO}-d_6$ ):  $\delta_{\text{C}}$  (ppm) 156.4, 149.1, 143.1, 141.7, 140.2, 139.2, 134.5, 129.9, 128.5, 127.8, 127.3, 126.7, 126.0, 122.9, 122.5, 120.6, 119.9, 119.1, 115.4, 109.9, 37.3, 13.8; HRMS (ESI-TOF,  $[\text{M}]^+$ ): calcd. 363.1855 for  $\text{C}_{26}\text{H}_{23}\text{N}_2^+$ , found 363.1854.

QCZ:  $^1\text{H}$  NMR (400 MHz,  $\text{DMSO}-d_6$ ):  $\delta_{\text{H}}$  (ppm) 8.6 (d,  $J = 8$ , 1H), 8.56 (s, 1H), 8.52 (d,  $J = 8.0$ , 1H), 8.34 (t,  $J = 14$ , 2H), 8.26 (dd,  $J = 8.0$ , 2H), 8.17–8.11 (m, 2H), 7.98 (s, 1H), 7.91 (t,  $J = 7.4$ , 1H), 7.79 (d,  $J = 8.0$ , 1H), 7.72 (d,  $J = 8.0$ , 1H), 7.55 (t,  $J = 7.6$ , 1H), 7.33 (t,  $J = 7.4$ , 1H), 4.56 (s, 3H), 4.52 (q,  $J = 8$ , 2H), 1.37 (t,  $J = 8$ , 3H);  $^{13}\text{C}$  NMR (100 MHz,  $\text{DMSO}-d_6$ ):  $\delta_{\text{C}}$  (ppm) 143.1, 140.2, 134.5, 129.9, 127.3, 120.6, 119.9, 115.4, 109.9, 37.3, 13.7; HRMS (ESI-TOF,  $[\text{M}]^+$ ): calcd. 363.1855 for  $\text{C}_{26}\text{H}_{23}\text{N}_2^+$ , found 363.1854.

**Isothermal Titration Calorimetry (ITC).** To ascertain the selectivity and thermodynamics of binding profiles of carbazole ligands for *c-MYC* and *BCL-2* GQ-forming sequences, we performed ITC using an iTTC200 Microcalorimeter at 25 °C. Oligonucleotide sequences and ligands were freshly prepared and degassed under vacuum for 10 min ahead of titration experiments to ensure the removal of bubbles, if any. The ligand solutions were diluted to a concentration of 20  $\mu\text{M}$  in 10 mM potassium phosphate buffer (10 mM  $\text{K}_2\text{HPO}_4$  + 10 mM  $\text{KH}_2\text{PO}_4$ ) containing 0.1 M KCl (pH 7.0). A syringe was filled with the quadruplex sequences (500  $\mu\text{M}$ ) present in the upstream promoter regions of *c-MYC* (Pu27), *BCL-2* (Pu30), *VEGF-A* (Pu22), *KRAS* (Pu32) oncogenes, rDNA-GQ, and duplex

DNA (Figure S20), which were injected at an interval of 150 s into the calorimeter cell containing 20  $\mu\text{M}$  carbazole ligands. The binding profile of Nucleolin and rDNA GQ was also monitored by titrating 500  $\mu\text{M}$  rDNA GQ in the cell containing 20  $\mu\text{M}$  purified Nucleolin. A control experiment was performed in parallel by injecting the same concentration of oligonucleotides into the identical buffer without small molecules to subtract the heat of dilution from ligand-quadruplex binding experiments before curve fitting (Figure S19). The number of injections was set at 20 or 30 to achieve the binding saturation. The heat of reaction per injection ( $\mu\text{cal/s}$ ) was determined by integration of the peak areas using in-built Origin 7.0 software, which provided the best-fit values of the enthalpy of binding ( $\Delta H$ ), the stoichiometry of binding ( $n$ ), and the dissociation constant ( $K_{\text{D}}$ ). Data points were further fitted with “one site” binding mode. The quality of the fitting curve was inspected by the reduced Chi-squared values ( $\chi^2_{\text{R}}$ ). TmPyP4 was used as a positive control to compare the binding profiles (Figure S21).

**Time-Resolved Fluorescence Spectroscopy.** Fluorescence lifetimes were performed on a Horiba Delta Flex time-correlated single photon counting (TCSPC) instrument. Lifetime measurements were carried out in 20 mM phosphate buffered saline (PBS) supplemented with 100 mM KCl at pH 7.4 using 1  $\mu\text{M}$  carbazole ligands incubated for 10 min at room temperature with different pre-annealed GQ (2  $\mu\text{M}$ ) and duplex DNAs (2  $\mu\text{M}$ ). A 480 nm nano-LED with a pulse repetition rate of 1 MHz was used as the light source. The instrument response function (IRF) was collected by using a scatterer (Ludox AS40 colloidal silica, Sigma-Aldrich). Fluorescence lifetime ( $\lambda_{\text{exc}} = 480$  nm) and gated emission were measured on an FLSP920 spectrometer (Edinburgh Instruments) equipped with a micro flash lamp ( $\mu\text{F}2$ ) setup. From the measured decay traces, the data were fitted with a multi-exponential decay, and  $\chi^2$  was less than 1.1. Notably, the lifetime is too short for the accurate fitting, which is suggestive of very weak emission intensity from TCA in PBS buffer.

**Dual-Luciferase Assays.** Dual-luciferase assays were performed to examine the intracellular selectivity of carbazole ligands (TCA, LCA, QCA, TCZ, LCZ, and QCZ) for different quadruplex-forming scaffolds in oncogene (*c-MYC*, *BCL-2*, *VEGF-A*, and *KRAS*) promoters. We also monitored the magnitudes of promoter repression by carbazole ligands in the MDAMB-231 cell line in contrast to the GQ-null promoter constructs of the corresponding oncogenes. Luciferase constructs having oncogene promoters (*c-MYC*, *BCL-2*, *KRAS*, and *VEGF-A*) of interest (with and without the GQ scaffolds) were transformed into One Shot Mach1 T1 competent *Escherichia coli* cells (Invitrogen). Transformed cells were harvested into Luria broth (LB) agar plates with 100  $\mu\text{g/mL}$  ampicillin and incubated at 37 °C for 8–9 h. A single colony was inoculated into a secondary bacterial culture overnight, and plasmids were isolated using a QIAprep Spin Miniprep Kit (Qiagen) for transfection. MDAMB-231 cells were subcultured into 24-well microtiter plates at a cell density of  $1 \times 10^5$  cells per well. A total of 500 ng of the reporter constructs (with and/or without quadruplex motifs)<sup>86</sup> driving the expression of Renilla luciferase were cotransfected with 50 ng of pGL3-control vectors (Promega) (used as internal control), encoding firefly luciferase into MDAMB-231 cells using the Lipofectamine 2000 transfection reagent (Thermo-Fisher Scientific) as per manufacturer's protocol. After 24 h of transfection, cells were treated with Carbazole ligands at an increasing concentration gradient. After 24 h post-treatment, MDAMB-231 cell lysate was prepared via passive lysis in 100  $\mu\text{L}$  1 $\times$  Passive lysis buffer (PLB) for 15 min at room temperature. Renilla and firefly luciferase activities in 25  $\mu\text{L}$  of MDAMB-231 cell lysate were estimated by a Dual-Luciferase reporter assay system (Promega) as per manufacturer's recommendations. Renilla luciferase enzyme activity was normalized to that of the firefly luciferase activity, and the luminescence of the treated samples was normalized to the untreated ones, which provided the estimate of fold change for Renilla luciferase activities by different quadruplex topologies in the presence and absence of the compounds. The luminescence of each sample was detected in Glo-Max 20/20 Single-Tube Luminometer (Promega) in

triplicates, and the luminescence of each sample was averaged from three independent studies.

**Chromatin Immunoprecipitation (ChIP).** Chromatin immunoprecipitation studies were performed to monitor the promoter occupancies of transcription factors (WT1, NM23-H2, and Nucleolin) on the quadruplex-forming regions at *c-MYC*, *BCL-2*, and rDNA promoters.<sup>88</sup> MDAMB-231 cells were grown in a 10 cm<sup>2</sup> culture flask at a density of  $2 \times 10^6$  cells per well and treated with carbazole ligands (TCA, LCA, QCA, TCZ, LCZ, and QCZ) for 24 h, whereas for rDNA ChIP analysis, MDAMB-231 cells were treated with either TCA or TCZ at 0.5, 1, and 2  $\mu$ M concentrations each and harvested at the end of 12 h. Cells were cross-linked with formaldehyde, harvested, lysed, and then chromatin-immunoprecipitated following the standard protocols published previously.<sup>94</sup> Eluted DNA was amplified by PCR (polymerase chain reaction) using forward and reverse primers (Table S1) specific to the quadruplex-enriched regions of *c-MYC* and *BCL-2* promoters and the Phusion High-Fidelity PCR Kit (NEB). Primary ChIP-grade antibodies used to immunoprecipitate chromatin included the ChIP-grade WT1 primary antibody (sc-192, Santa Cruz), NM23-H2 (L-15) antibody (sc-14790, Santa Cruz), and Anti-Nucleolin antibody [4E2] (ChIP grade) (Abcam). However, anti-rabbit IgG was employed for mock immunoprecipitation. Primer sequences used in the PCR are given in Table S2. For treatment with recombinant NM23-H2, we exogenously treated the cells with recombinant NM23-H2 having a MYC-DDK tag as NM23-H2 is known to permeate the plasma membrane by endocytosis using GTP hydrolysis and dynamin. We confirmed its localization in MDAMB-231 cells by immunoprecipitation with the anti-MYC-DDK antibody following a previously published protocol (Figure S18).

**Ribosomal Biogenesis.** Cells were treated with either TCA or TCZ for 24 h, and total RNA was extracted using a TRIZOL reagent as per the manufacturer's guidelines. cDNA was prepared with 1  $\mu$ g of total RNA using the Revert Aid cDNA synthesis kit (Thermo) as per manual in 25  $\mu$ L reaction volume. All cDNA samples were aliquoted and stored at  $-20$  °C until further use. Cells were treated with either TCA or TCZ each at three different concentrations 0.5, 1, and 2  $\mu$ M each for 12 h. Gene expressions for 28S rRNA, 18S rRNA, 5.8S rRNA, 45S rRNA, and 47S rRNA at 12 h time points were measured. Reactions (25  $\mu$ L) were set up using the Takara PCR kit as per the manufacturer's protocols. Primer sequences are provided in Table S2.

## ■ ASSOCIATED CONTENT

### SI Supporting Information

The Supporting Information is available free of charge at <https://pubs.acs.org/doi/10.1021/acsbiochemau.1c00039>.

Experimental methods, absorbance and fluorescence spectra, ITC binding profiles, CD thermal melting data, NMR titration spectra, molecular docking, simulation figures, and NMR and HRMS characterization data (PDF)

## ■ AUTHOR INFORMATION

### Corresponding Authors

**Subhrangsu Chatterjee** – Department of Biophysics, Bose Institute, Kolkata 700054, India; [orcid.org/0000-0002-3250-7311](https://orcid.org/0000-0002-3250-7311); Email: [subhrangsu@gmail.com](mailto:subhrangsu@gmail.com)

**Thimmaiah Govindaraju** – Bioorganic Chemistry Laboratory, New Chemistry Unit, Jawaharlal Nehru Centre for Advanced Scientific Research (JNCASR), Bengaluru, Karnataka 560064, India; [orcid.org/0000-0002-9423-4275](https://orcid.org/0000-0002-9423-4275); Email: [tgaju@jncasr.ac.in](mailto:tgaju@jncasr.ac.in)

## Authors

**Yelisetty Venkata Suseela** – Bioorganic Chemistry Laboratory, New Chemistry Unit, Jawaharlal Nehru Centre for Advanced Scientific Research (JNCASR), Bengaluru, Karnataka 560064, India; [orcid.org/0000-0003-3590-570X](https://orcid.org/0000-0003-3590-570X)

**Pallabi Sengupta** – Department of Biophysics, Bose Institute, Kolkata 700054, India

**Tanaya Roychowdhury** – Cancer Biology and Inflammatory Disorder Division, CSIR-Indian Institute of Chemical Biology, Kolkata 700032, India

**Suman Panda** – Department of Biophysics, Bose Institute, Kolkata 700054, India

**Sangita Talukdar** – Bioorganic Chemistry Laboratory, New Chemistry Unit, Jawaharlal Nehru Centre for Advanced Scientific Research (JNCASR), Bengaluru, Karnataka 560064, India

**Samit Chattopadhyay** – Cancer Biology and Inflammatory Disorder Division, CSIR-Indian Institute of Chemical Biology, Kolkata 700032, India

Complete contact information is available at:

<https://pubs.acs.org/10.1021/acsbiochemau.1c00039>

## Author Contributions

†V.S.Y., S.P., and R.T. contributed equally. All authors have given approval to the final version of the manuscript.

## Funding

We thank JNCASR, BRICS Multilateral R&D Project (grant: DST/IMRCD/BRIC/PilotCALL2/EPNAPT/2018(G)), and Swarnajayanti Fellowship (grant: DST/SJF/CSA-02/2015-2016), the Department of Science and Technology (DST), Govt. of India. S.C. thanks DST (EMR/2015/002186), DBT-SyMeC, and Council of Scientific and Industrial Research, Govt. of India for funding.

## Notes

The authors declare no competing financial interest.

## ■ ACKNOWLEDGMENTS

We are thankful to Prof. S. Balasubramanian, CPMU, JNCASR for the lab facility to run MD simulation and Mr. Sounak Bhattacharya for the Leica SP8 Super-resolution confocal microscope, Central Instrumentation Facility, IICB.

## ■ ABBREVIATIONS

BMVC	3,6-bis(1-methyl-4-vinylpyridinium) carbazole diiodide
ChIP	chromatin immunoprecipitation
FITC/PI	fluorescein isothiocyanate/propidium iodide
IRES	internal ribosome entry site
ITC	isothermal titration calorimetry
NCL	Nucleolin
PARP	poly(ADP-ribose) polymerase
Sp1	specificity protein 1
WT1	Wilm's tumor 1

## ■ REFERENCES

- Hänsel-Hertsch, R.; Di Antonio, M.; Balasubramanian, S. DNA G-quadruplexes in the human genome: detection, functions and therapeutic potential. *Nat. Rev. Mol. Cell Biol.* **2017**, *18*, 279.
- Neidle, S.; Balasubramanian, S., *Quadruplex nucleic acids*; Royal Society of Chemistry: 2007; Vol. 7.

- (3) Sen, D.; Gilbert, W. Formation of parallel four-stranded complexes by guanine-rich motifs in DNA and its implications for meiosis. *Nature* **1988**, *334*, 364.
- (4) Kumari, S.; Bugaut, A.; Huppert, J. L.; Balasubramanian, S. An RNA G-quadruplex in the 5' UTR of the NRAS proto-oncogene modulates translation. *Nat. Chem. Biol.* **2007**, *3*, 218–221.
- (5) Drygin, D.; Siddiqui-Jain, A.; O'Brien, S.; Schwaebe, M.; Lin, A.; Bliesath, J.; Ho, C. B.; Proffitt, C.; Trent, K.; Whitten, J. P.; Lim, J. K. C.; von Hoff, D.; Anderes, K.; Rice, W. G. Anticancer activity of CX-3543: a direct inhibitor of rRNA biogenesis. *Cancer Res.* **2009**, *69*, 7653–7661.
- (6) Balasubramanian, S.; Hurley, L. H.; Neidle, S. Targeting G-quadruplexes in gene promoters: a novel anticancer strategy? *Nat. Rev. Drug Discov.* **2011**, *10*, 261–275.
- (7) Paeschke, K.; Capra, J. A.; Zakian, V. A. DNA replication through G-quadruplex motifs is promoted by the *Saccharomyces cerevisiae* Pif1 DNA helicase. *Cell* **2011**, *145*, 678–691.
- (8) Lemmens, B.; van Schendel, R.; Tijsterman, M. Mutagenic consequences of a single G-quadruplex demonstrate mitotic inheritance of DNA replication fork barriers. *Nat. Commun.* **2015**, *6*, 8909.
- (9) Lam, E. Y. N.; Beraldi, D.; Tannahill, D.; Balasubramanian, S. G-quadruplex structures are stable and detectable in human genomic DNA. *Nat. Commun.* **2013**, *4*, 1796.
- (10) Suseela, Y. V.; Narayanaswamy, N.; Pratihari, S.; Govindaraju, T. Far-red fluorescent probes for canonical and non-canonical nucleic acid structures: current progress and future implications. *Chem. Soc. Rev.* **2018**, *47*, 1098–1131.
- (11) Biffi, G.; Tannahill, D.; McCafferty, J.; Balasubramanian, S. Quantitative visualization of DNA G-quadruplex structures in human cells. *Nat. Chem.* **2013**, *5*, 182.
- (12) Henderson, A.; Wu, Y.; Huang, Y. C.; Chavez, E. A.; Platt, J.; Johnson, F. B.; Brosh, R. M.; Sen, D.; Lansdorp, P. M. Detection of G-quadruplex DNA in mammalian cells. *Nucleic Acids Res.* **2014**, *42*, 860–869.
- (13) Hansel-Hertsch, R.; Beraldi, D.; Lensing, S. V.; Marsico, G.; Zyner, K.; Parry, A.; Di Antonio, M.; Pike, J.; Kimura, H.; Narita, M.; Tannahill, D.; Balasubramanian, S. G-quadruplex structures mark human regulatory chromatin. *Nat. Genet.* **2016**, *48*, 1267–1272.
- (14) Laguerre, A.; Hukezalie, K.; Winckler, P.; Katranji, F.; Chanteloup, G.; Pirrotta, M.; Perrier-Cornet, J.-M.; Wong, J. M. Y.; Monchaud, D. Visualization of RNA-Quadruplexes in live cells. *J. Am. Chem. Soc.* **2015**, *137*, 8521–8525.
- (15) Shivalingam, A.; Izquierdo, M. A.; Marois, A. L.; Vyšniauskas, A.; Suhling, K.; Kuimova, M. K.; Vilar, R. The interactions between a small molecule and G-quadruplexes are visualized by fluorescence lifetime imaging microscopy. *Nat. Commun.* **2015**, *6*, 8178.
- (16) Schnell, U.; Dijk, F.; Sjollem, K. A.; Giepmans, B. N. G. Immunolabeling artifacts and the need for live-cell imaging. *Nat. Methods* **2012**, *9*, 152–158.
- (17) Schmiedeberg, L.; Skene, P.; Deaton, A.; Bird, A. A temporal threshold for formaldehyde crosslinking and fixation. *PLoS One* **2009**, *4*, No. e4636.
- (18) Di Antonio, M.; Ponjavic, A.; Radzevičius, A.; Ranasinghe, R. T.; Catalano, M.; Zhang, X.; Shen, J.; Needham, L.-M.; Lee, S. F.; Klenerman, D.; Balasubramanian, S. Single-molecule visualization of DNA G-quadruplex formation in live cells. *Nat. Chem.* **2020**, *12*, 832–837.
- (19) Largy, E.; Granzhan, A.; Hamon, F.; Verga, D.; Teulade-Fichou, M. P. Visualizing the Quadruplex: From Fluorescent Ligands to Light-Up Probes. *Top. Curr. Chem.* **2012**, *330*, 111–177.
- (20) Vummidhi, B. R.; Alzeer, J.; Luedtke, N. W. Fluorescent Probes for G-Quadruplex Structures. *Chem. Bio. Chem.* **2013**, *14*, 540–558.
- (21) Xu, S.; Li, Q.; Xiang, J.; Yang, Q.; Sun, H.; Guan, A.; Wang, L.; Liu, Y.; Yu, L.; Shi, Y.; Chen, H.; Tang, Y. Directly lighting up RNA G-quadruplexes from test tubes to living human cells. *Nucleic Acids Res.* **2015**, *43*, 9575–9586.
- (22) Chen, S.-B.; Hu, M.-H.; Liu, G.-C.; Wang, J.; Ou, T.-M.; Gu, L.-Q.; Huang, Z.-S.; Tan, J.-H. Visualization of NRAS RNA G-quadruplex structures in cells with an engineered fluorogenic hybridization probe. *J. Am. Chem. Soc.* **2016**, *138*, 10382–10385.
- (23) Huang, W.-C.; Tseng, T.-Y.; Chen, Y.-T.; Chang, C.-C.; Wang, Z.-F.; Wang, C.-L.; Hsu, T.-N.; Li, P.-T.; Chen, C.-T.; Lin, J.-J.; Lou, P. J.; Chang, T. C. Direct evidence of mitochondrial G-quadruplex DNA by using fluorescent anti-cancer agents. *Nucleic Acids Res.* **2015**, *43*, 10102–10113.
- (24) Suseela, Y. V.; Satha, P.; Murugan, N. A.; Govindaraju, T. Recognition of G-quadruplex topology through hybrid binding with implications in cancer theranostics. *Theranostics* **2020**, *10*, 10394–10414.
- (25) Suseela, Y. V.; Satha, P.; Govindaraju, T. Mitochondria-Specific Recognition of G-Quadruplexes by a Flavylum-Based Turn-On Near-Infrared Rotor Probe. *Analysis & Sensing* **2021**, *1*, 180–187.
- (26) Liu, L.-Y.; Liu, W.; Wang, K.-N.; Zhu, B.-C.; Xia, X.-Y.; Ji, L.-N.; Mao, Z.-W. Quantitative Detection of G-Quadruplex DNA in Live Cells Based on Photon Counts and Complex Structure Discrimination. *Angew. Chem., Int. Ed.* **2020**, *59*, 9719–9726.
- (27) Chen, H.; Liu, H. D.; Qing, G. L. Targeting oncogenic Myc as a strategy for cancer treatment. *Signal Transduction Targeted Ther.* **2018**, *3*, 5.
- (28) Cory, S.; Huang, D. C. S.; Adams, J. M. The Bcl-2 family: roles in cell survival and oncogenesis. *Oncogene* **2003**, *22*, 8590–8607.
- (29) Fallah, Y.; Brundage, J.; Allegakoen, P.; Shajahan-Haq, A. N. MYC-driven pathways in breast cancer subtypes. *Biomolecules* **2017**, *7*, 53.
- (30) Shivakumar, L.; Armitage, J. O. Bcl-2 gene expression as a predictor of outcome in diffuse large B-cell lymphoma. *Clin Lymphoma Myeloma* **2006**, *6*, 455–457.
- (31) Sasaki, N.; Kuroda, J.; Nagoshi, H.; Yamamoto, M.; Kobayashi, S.; Tsutsumi, Y.; Kobayashi, T.; Shimura, Y.; Matsumoto, Y.; Taki, T.; Nishida, K.; Horiike, S.; Akao, Y.; Taniwaki, M. Bcl-2 is a better therapeutic target than c-Myc, but attacking both could be a more effective treatment strategy for B-cell lymphoma with concurrent Bcl-2 and c-Myc overexpression. *Exp. Hematol.* **2011**, *39*, 817–828.e1.
- (32) Ting, C. Y.; Chang, K. M.; Kuan, J. W.; Sathar, J.; Chew, L. P.; Wong, O. L. J.; Yusuf, Y.; Wong, L.; Samsudin, A. T.; Pana, M. N. B.; Lees, S. K.; Gopal, N. S. R.; Puri, R.; Ong, T. C.; Bahari, S. K.; Goh, A. S.; Teoh, C. S. Clinical Significance of BCL2, C-MYC, and BCL6 Genetic Abnormalities, Epstein-Barr Virus Infection, CD5 Protein Expression, Germinal Center B Cell/Non-Germinal Center B-Cell Subtypes, Co-expression of MYC/BCL2 Proteins and Co-expression of MYC/BCL2/BCL6 Proteins in Diffuse Large B-Cell Lymphoma: A Clinical and Pathological Correlation Study of 120 Patients. *Int. J. Med. Sci.* **2019**, *16*, 556–566.
- (33) Godfrey, J. K.; Nabhan, C.; Karrison, T.; Kline, J. P.; Cohen, K. S.; Bishop, M. R.; Stadler, W. M.; Karmali, R.; Venugopal, P.; Rapoport, A. P.; Smith, S. M. Phase 1 study of lenalidomide plus dose-adjusted EPOCH-R in patients with aggressive B-cell lymphomas with deregulated MYC and BCL2. *Cancer* **2019**, *125*, 1830–1836.
- (34) Han, Z.; Liang, J.; Li, Y.; He, J. Drugs and Clinical Approaches Targeting the Antiapoptotic Protein: A Review. *Biomed Res. Int.* **2019**, *2019*, 1212369.
- (35) Jin, F.; Yu, C.; Lai, L.; Liu, Z. Ligand clouds around protein clouds: a scenario of ligand binding with intrinsically disordered proteins. *PLoS Comput. Biol.* **2013**, *9*, No. e1003249.
- (36) Fresquet, V.; Rieger, M.; Carolis, C.; García-Barchino, M. J.; Martínez-Climent, J. A. Acquired mutations in BCL2 family proteins conferring resistance to the BH3 mimetic ABT-199 in lymphoma. *Blood* **2014**, *123*, 4111–4119.
- (37) Beale, P. J.; Rogers, P.; Boxall, F.; Sharp, S. Y.; Kelland, L. R. BCL-2 family protein expression and platinum drug resistance in ovarian carcinoma. *Br. J. Cancer* **2000**, *82*, 436–440.
- (38) Yang, D.; Hurley, L. H. Structure of the biologically relevant G-quadruplex in the c-MYC promoter. *Nucleosides, Nucleotides Nucleic Acids* **2006**, *25*, 951–968.
- (39) Agrawal, P.; Lin, C.; Mathad, R. I.; Carver, M.; Yang, D. Z. The Major G-Quadruplex Formed in the Human BCL-2 Proximal

Promoter Adopts a Parallel Structure with a 13-nt Loop in K+ Solution. *J. Am. Chem. Soc.* **2014**, *136*, 1750–1753.

(40) Sengupta, P.; Chattopadhyay, S.; Chatterjee, S. G-Quadruplex surveillance in BCL-2 gene: a promising therapeutic intervention in cancer treatment. *Drug Discovery Today* **2017**, *22*, 1165–1186.

(41) Asamitsu, S.; Obata, S.; Yu, Z.; Bando, T.; Sugiyama, H. Recent progress of targeted G-quadruplex-preferred ligands toward cancer therapy. *Molecules* **2019**, *24*, 429.

(42) Francisco, A. P.; Paulo, A. Oncogene Expression Modulation in Cancer Cell Lines by DNA G-Quadruplex-Interactive Small Molecules. *Curr. Med. Chem.* **2018**, *24*, 4873–4904.

(43) Vasan, N.; Baselga, J.; Hyman, D. M. A view on drug resistance in cancer. *Nature* **2019**, *575*, 299–309.

(44) Bastide, A.; David, A. The ribosome, (slow) beating heart of cancer (stem) cell. *Oncogenesis* **2018**, *7*, 34.

(45) Kim, J. H.; You, K. R.; Kim, I. H.; Cho, B. H.; Kim, C. Y.; Kim, D. G. Over-expression of the ribosomal protein L36a gene is associated with cellular proliferation in hepatocellular carcinoma. *Hepatology* **2004**, *39*, 129–138.

(46) Yang, S.; Cui, J.; Yang, Y.; Liu, Z.; Yan, H.; Tang, C.; Wang, H.; Qin, H.; Li, X.; Li, J.; Wang, W.; Huang, Y.; Gao, H. Over-expressed RPL34 promotes malignant proliferation of non-small cell lung cancer cells. *Gene* **2016**, *576*, 421–428.

(47) van Riggelen, J.; Yetil, A.; Felsher, D. W. MYC as a regulator of ribosome biogenesis and protein synthesis. *Nat. Rev. Cancer* **2010**, *10*, 301–309.

(48) Barna, M.; Pusic, A.; Zollo, O.; Costa, M.; Kondrashov, N.; Rego, E.; Rao, P. H.; Ruggero, D. Suppression of Myc oncogenic activity by ribosomal protein haploinsufficiency. *Nature* **2008**, *456*, 971–975.

(49) Shi, Y.; Yang, Y.; Hoang, B.; Bardeleben, C.; Holmes, B.; Gera, J.; Lichtenstein, A. Therapeutic potential of targeting IRES-dependent c-myc translation in multiple myeloma cells during ER stress. *Oncogene* **2016**, *35*, 1015–1024.

(50) Hertz, M. I.; Landry, D. M.; Willis, A. E.; Luo, G.; Thompson, S. R. Ribosomal Protein S25 Dependency Reveals a Common Mechanism for Diverse Internal Ribosome Entry Sites and Ribosome Shunting. *Mol. Cell. Biol.* **2013**, *33*, 1016–1026.

(51) Yuan, J.-H.; Shao, W.; Chen, S.-B.; Huang, Z.-S.; Tan, J.-H. Recent advances in fluorescent probes for G-quadruplex nucleic acids. *Biochem. Biophys. Res. Commun.* **2020**, *531*, 18–24.

(52) Jamroskovic, J.; Doimo, M.; Chand, K.; Obi, I.; Kumar, R.; Brännström, K.; Hedenström, M.; Nath Das, R.; Akhunzianov, A.; Deiana, M.; Kasho, K.; Sulis Sato, S.; Pourbozorgi, P. L.; Mason, J. E.; Medini, P.; Öhlund, D.; Wanrooij, S.; Chorell, E.; Sabouri, N. Quinazoline Ligands Induce Cancer Cell Death through Selective STAT3 Inhibition and G-Quadruplex Stabilization. *J. Am. Chem. Soc.* **2020**, *142*, 2876–2888.

(53) Feng, X. J.; Wu, P. L.; Bolze, F.; Leung, H. W. C.; Li, K. F.; Mak, N. K.; Kwong, D. W. J.; Nicoud, J.-F.; Cheah, K. W.; Wong, M. S. Cyanines as new fluorescent probes for DNA detection and two-photon excited bioimaging. *Org. Lett.* **2010**, *12*, 2194–2197.

(54) Tseng, T.-Y.; Wang, Z.-F.; Chien, C.-H.; Chang, T.-C. In-cell optical imaging of exogenous G-quadruplex DNA by fluorogenic ligands. *Nucleic Acids Res.* **2013**, *41*, 10605–10618.

(55) Vargas, R.; Garza, J.; Dixon, D. A.; Hay, B. P. How Strong Is the C $\alpha$ -H $\cdots$ OC Hydrogen Bond? *J. Am. Chem. Soc.* **2000**, *122*, 4750–4755.

(56) Bohnuud, T.; Beglov, D.; Ngan, C. H.; Zerbe, B.; Hall, D. R.; Brenke, R.; Vajda, S.; Frank-Kamenetskii, M. D.; Kozakov, D. Computational mapping reveals dramatic effect of Hoogsteen breathing on duplex DNA reactivity with formaldehyde. *Nucleic Acids Res.* **2012**, *40*, 7644–7652.

(57) Tsutsumi, L. S.; Gündisch, D.; Sun, D. Carbazole scaffold in medicinal chemistry and natural products: a review from 2010-2015. *Curr. Top. Med. Chem.* **2016**, *16*, 1290–1313.

(58) Maji, B.; Kumar, K.; Kaulage, M.; Muniyappa, K.; Bhattacharya, S. Design and Synthesis of New Benzimidazole–Carbazole Conjugates for the Stabilization of Human Telomeric DNA, Telomerase

Inhibition, and Their Selective Action on Cancer Cells. *J. Med. Chem.* **2014**, *57*, 6973–6988.

(59) Kaulage, M. H.; Maji, B.; Pasadi, S.; Ali, A.; Bhattacharya, S.; Muniyappa, K. Targeting G-quadruplex DNA structures in the telomere and oncogene promoter regions by benzimidazole–carbazole ligands. *Eur. J. Med. Chem.* **2018**, *148*, 178–194.

(60) Maji, B.; Kumar, K.; Muniyappa, K.; Bhattacharya, S. New dimeric carbazole–benzimidazole mixed ligands for the stabilization of human telomeric G-quadruplex DNA and as telomerase inhibitors. A remarkable influence of the spacer. *Org. Biomol. Chem.* **2015**, *13*, 8335–8348.

(61) Issa, S.; Prandina, A.; Bedel, N.; Rongved, P.; Yous, S.; Le Borgne, M.; Bouaziz, Z. Carbazole scaffolds in cancer therapy: a review from 2012 to 2018. *J. Enzyme Inhib. Med. Chem.* **2019**, *34*, 1321–1346.

(62) Gluszyńska, A.; Juskowiak, B.; Kuta-Siejkowska, M.; Hoffmann, M.; Haider, S. Carbazole ligands as c-myc G-quadruplex binders. *Int. J. Biol. Macromol.* **2018**, *114*, 479–490.

(63) Narayanaswamy, N.; Das, S.; Samanta, P. K.; Banu, K.; Sharma, G. P.; Mondal, N.; Dhar, S. K.; Pati, S. K.; Govindaraju, T. Sequence-specific recognition of DNA minor groove by an NIR-fluorescence switch-on probe and its potential applications. *Nucleic Acids Res.* **2015**, *43*, 8651–8663.

(64) Narayanaswamy, N.; Narra, S.; Nair, R. R.; Saini, D. K.; Kondaiah, P.; Govindaraju, T. Stimuli-responsive colorimetric and NIR fluorescence combination probe for selective reporting of cellular hydrogen peroxide. *Chem. Sci.* **2016**, *7*, 2832–2841.

(65) Ertl, P.; Rohde, B.; Selzer, P. Fast Calculation of Molecular Polar Surface Area as a Sum of Fragment-Based Contributions and Its Application to the Prediction of Drug Transport Properties. *J. Med. Chem.* **2000**, *43*, 3714–3717.

(66) Agrawal, P.; Hatzakis, E.; Guo, K.; Carver, M.; Yang, D. Solution structure of the major G-quadruplex formed in the human VEGF promoter in K<sup>+</sup>: insights into loop interactions of the parallel G-quadruplexes. *Nucleic Acids Res.* **2013**, *41*, 10584–10592.

(67) Cogo, S.; Xodo, L. E. G-quadruplex formation within the promoter of the KRAS proto-oncogene and its effect on transcription. *Nucleic Acids Res.* **2006**, *34*, 2536–2549.

(68) Liu, W.; Lin, C.; Wu, G.; Dai, J.; Chang, T.-C.; Yang, D. Structures of 1:1 and 2:1 complexes of BMVC and MYC promoter G-quadruplex reveal a mechanism of ligand conformation adjustment for G4-recognition. *Nucleic Acids Res.* **2019**, *47*, 11931–11942.

(69) Kumar, R.; Chand, K.; Bhowmik, S.; Das, R. N.; Bhattacharjee, S.; Hedenström, M.; Chorell, E. Subtle structural alterations in G-quadruplex DNA regulate site specificity of fluorescence light-up probes. *Nucleic Acids Res.* **2020**, *48*, 1108–1119.

(70) Gluszyńska, A.; Juskowiak, B.; Kuta-Siejkowska, M.; Hoffmann, M.; Haider, S. Carbazole Derivatives' Binding to c-KIT G-Quadruplex DNA. *Molecules* **2018**, *23*, 1134.

(71) Suseela, Y. V.; Das, S.; Pati, S. K.; Govindaraju, T. Imidazolyl-Naphthalenediimide-Based Threading Intercalators of DNA. *Chem. Bio. Chem.* **2016**, *17*, 2162–2171.

(72) Peng, X.; Song, F.; Lu, E.; Wang, Y.; Zhou, W.; Fan, J.; Gao, Y. Heptamethine Cyanine Dyes with a Large Stokes Shift and Strong Fluorescence: A Paradigm for Excited-State Intramolecular Charge Transfer. *J. Am. Chem. Soc.* **2005**, *127*, 4170–4171.

(73) Mohanty, J.; Barooah, N.; Dhamodharan, V.; Harikrishna, S.; Pradeepkumar, P. I.; Bhasikuttan, A. C. Thioflavin T as an Efficient Inducer and Selective Fluorescent Sensor for the Human Telomeric G-Quadruplex DNA. *J. Am. Chem. Soc.* **2013**, *135*, 367–376.

(74) Planas-Silva, M. D.; Bruggeman, R. D.; Grenko, R. T.; Smith, J. Overexpression of c-Myc and Bcl-2 during progression and distant metastasis of hormone-treated breast cancer. *Exp. Mol. Pathol.* **2007**, *82*, 85–90.

(75) Liu, H.; Radisky, D. C.; Yang, D.; Xu, R.; Radisky, E. S.; Bissell, M. J.; Bishop, J. M. MYC suppresses cancer metastasis by direct transcriptional silencing of  $\alpha$ , and  $\beta$ , integrin subunits. *Nat. Cell Biol.* **2012**, *14*, 567–574.

- (76) Roy, S.; Ali, A.; Kamra, M.; Muniyappa, K.; Bhattacharya, S. Specific stabilization of promoter G-Quadruplex DNA by 2,6-disubstituted amidoanthracene-9,10-dione based dimeric distamycin analogues and their selective cancer cell cytotoxicity. *Eur. J. Med. Chem.* **2020**, *195*, 112202.
- (77) Dutta, A.; Banerjee, N.; Sengupta, P.; Chatterjee, S.; Chattopadhyay, S.; Roychowdhury, T. Site-specific amino acid substitution in dodecameric peptides determines the stability and unfolding of c-MYC quadruplex promoting apoptosis in cancer cells. *Nucleic Acids Res.* **2018**, *46*, 9932–9950.
- (78) Cogoi, S.; Paramasivam, M.; Membrino, A.; Yokoyama, K. K.; Xodo, L. E. The KRAS Promoter Responds to Myc-associated Zinc Finger and Poly(ADP-ribose) Polymerase 1 Proteins, Which Recognize a Critical Quadruplex-forming GA-element\*. *J. Biol. Chem.* **2010**, *285*, 22003–22016.
- (79) Dai, J.; Chen, D.; Jones, R. A.; Hurley, L. H.; Yang, D. NMR solution structure of the major G-quadruplex structure formed in the human BCL2 promoter region. *Nucleic Acids Res.* **2006**, *34*, 5133–5144.
- (80) Gallagher, K.; Sharp, K. Electrostatic Contributions to Heat Capacity Changes of DNA-Ligand Binding. *Biophys. J.* **1998**, *75*, 769–776.
- (81) Sengupta, P.; Chatterjee, S. Inosine 5'-diphosphate, a molecular decoy rescues Nucleoside diphosphate kinase from c-MYC G-Quadruplex unfolding. *Biochim. Biophys. Acta, Gen. Subj.* **2020**, *1864*, 129649.
- (82) Ma, D.-L.; Chan, D. S.-H.; Fu, W.-C.; He, H.-Z.; Yang, H.; Yan, S.-C.; Leung, C.-H. Discovery of a natural product-like c-myc G-quadruplex DNA groove-binder by molecular docking. *PLoS One* **2012**, *7*, No. e43278.
- (83) Sutherland, C.; Cui, Y.; Mao, H.; Hurley, L. H. A mechanosensor mechanism controls the G-Quadruplex/i-Motif molecular switch in the MYC promoter NHE III<sub>1</sub>. *J. Am. Chem. Soc.* **2016**, *138*, 14138–14151.
- (84) Shan, C.; Lin, J.; Hou, J.-Q.; Liu, H.-Y.; Chen, S.-B.; Chen, A.-C.; Ou, T.-M.; Tan, J.-H.; Li, D.; Gu, L.-Q.; Huang, Z.-S. Chemical intervention of the NM23-H2 transcriptional programme on c-MYC via a novel small molecule. *Nucleic Acids Res.* **2015**, *43*, 6677–6691.
- (85) González, V.; Hurley, L. H. The C-Terminus of Nucleolin Promotes the Formation of the c-MYC G-Quadruplex and Inhibits c-MYC Promoter Activity. *Biochemistry* **2010**, *49*, 9706–9714.
- (86) Sengupta, P.; Bhattacharya, A.; Sa, G.; Das, T.; Chatterjee, S. Truncated G-quadruplex isomers cross-talk with the transcription factors to maintain homeostatic equilibria in c-MYC transcription. *Biochemistry* **2019**, *58*, 1975–1991.
- (87) Wang, X.-D.; Ou, T.-M.; Lu, Y.-J.; Li, Z.; Xu, Z.; Xi, C.; Tan, J.-H.; Huang, S.-L.; An, L.-K.; Li, D.; Gu, L.-Q.; Huang, Z.-S. Turning off Transcription of the bcl-2 Gene by Stabilizing the bcl-2 Promoter Quadruplex with Quindoline Derivatives. *J. Med. Chem.* **2010**, *53*, 4390–4398.
- (88) Xiong, Y.-X.; Chen, A.-C.; Yao, P.-F.; Zeng, D.-Y.; Lu, Y.-J.; Tan, J.-H.; Huang, Z.-S.; Ou, T.-M. Blocking the binding of WT1 to bcl-2 promoter by G-quadruplex ligand SYUIQ-FM05. *Biochem. Biophys. Rep.* **2016**, *5*, 346–352.
- (89) Catez, F.; Dalla Venezia, N.; Marcel, V.; Zorbas, C.; Lafontaine, D. L. J.; Diaz, J.-J. Ribosome biogenesis: An emerging druggable pathway for cancer therapeutics. *Biochem. Pharmacol.* **2019**, *159*, 74–81.
- (90) Lindström, M. S.; Jurada, D.; Bursac, S.; Orsolich, I.; Bartek, J.; Volarevic, S. Nucleolus as an emerging hub in maintenance of genome stability and cancer pathogenesis. *Oncogene* **2018**, *37*, 2351–2366.
- (91) Cong, R.; Das, S.; Ugrinova, I.; Kumar, S.; Mongelard, F.; Wong, J.; Bouvet, P. Interaction of nucleolin with ribosomal RNA genes and its role in RNA polymerase I transcription. *Nucleic Acids Res.* **2012**, *40*, 9441–9454.
- (92) Dai, M. S.; Lu, H. Crosstalk between c-Myc and ribosome in ribosomal biogenesis and cancer. *J. Cell. Biochem.* **2008**, *105*, 670–677.
- (93) Narayanaswamy, N.; Kumar, M.; Das, S.; Sharma, R.; Samanta, P. K.; Pati, S. K.; Dhar, S. K.; Kundu, T. K.; Govindaraju, T. A Thiazole Coumarin (TC) Turn-On Fluorescence Probe for AT-Base Pair Detection and Multipurpose Applications in Different Biological Systems. *Sci. Rep.* **2014**, *4*, 6476.
- (94) Zhang, X.; Su, J.; Jeong, M.; Ko, M.; Huang, Y.; Park, H. J.; Guzman, A.; Lei, Y.; Huang, Y.-H.; Rao, A.; Li, W.; Goodell, M. A. DNMT3A and TET2 compete and cooperate to repress lineage-specific transcription factors in hematopoietic stem cells. *Nat. Genet.* **2016**, *48*, 1014.